Geochimica et Cosmochimica Acta 358 (2023) 134–147

Contents lists available at ScienceDirect

Geochimica et Cosmochimica Acta

journal homepage: www.elsevier.com/locate/gca

Experimental and theoretical investigations of stable Sr isotope fractionation during its incorporation in aragonite

Jean-Michel Brazier [a,1], Marc Blanchard [b], Merlin Méheut [b], Anne-Désirée Schmitt [c], Jacques Schott [b], Vasileios Mavromatis (Βασίλειος Μαυρομάτης) [b,d,*,1]

[a] Institute of Applied Geosciences, Graz University of Technology, Rechbauerstrasse 12, 8010 Graz, Austria
[b] Geosciences Environnement Toulouse (GET), Observatoire Midi-Pyrénées, Université de Toulouse, CNRS, IRD, UPS, 14 Avenue Edouard Belin, 31400 Toulouse, France
[c] Université de Strasbourg, CNRS, ENGEES, ITES UMR 7063, 5, rue Descartes, 67084 Strasbourg Cédex, France
[d] Institute of Geological Sciences, University of Bern, Baltzerstr. 1+3, 3012 Bern, Switzerland

ARTICLE INFO

Associate editor: Andrew Jacobson

Keywords:
Aragonite
Stable Sr isotopes
First-principles calculations
Equilibrium fractionation

ABSTRACT

Strontium partitioning and isotope fractionation between aragonite and fluid have been determined experimentally at low values of the fluid saturation state (Ω) with respect to this mineral ($1.1 \leq \Omega_{aragonite} \leq 2.2$), and the measured isotope fractionation has been compared with the results of first-principles simulations. For the latter, Density Functional Theory (DFT) was used for estimation of the equilibrium Sr isotope fractionation between aragonite and Sr^{2+}(aq). The obtained results suggest that, for values of $\Omega_{aragonite}$ close to unity, the apparent distribution coefficient of Sr in aragonite ($D_{Sr,aragonite} = \frac{X_{SrCO_3}}{X_{CaCO_3}}\left(\frac{[Ca]}{[Sr]}\right)_{fluid}$) exhibits values higher than one that rapidly decrease at increasing aragonite growth rate. Under equilibrium conditions (i.e. $\Omega_{aragonite}$=1) a $D_{Sr,aragoinite}$ value of 2.7 can be extrapolated. Additionally, for aragonite growth rates $r_p \leq 10^{-8.0\pm0.2}$ (mol/m^2/s) the Sr isotope fractionation between aragonite and the fluid (i.e. $\Delta^{88/86}Sr_{aragonite\text{-}fluid}$) shows a constant value of −0.1 ±0.05‰, whereas it decreases to −0.40‰ when the growth rate increases to $10^{-7.7}$(mol/m^2/s). The surface reaction kinetic model (SRKM) developed by DePaolo (2011) has been used to describe the dependence of $D_{Sr,aragonite}$ and $\Delta^{88/86}Sr_{aragonite\text{-}fluid}$ on mineral growth rate. In this model the best fit for $D_{Sr,aragonite}$ and $\Delta^{88/86}Sr_{aragonite\text{-}fluid}$ were 4 and −0.01‰, respectively, whereas the kinetic isotope fractionation factor for $\Delta^{88/86}Sr_{aragonite\text{-}fluid}$ was −0.6‰. The results of first-principles calculations yield an equilibrium Sr isotope fractionation factor of −0.04‰ which is in excellent agreement with the experimental value of the present study. These results are the first experimental measurements of Sr isotope fractionation during inorganic aragonite precipitation as a function of growth rate and the first DFT calculations of Sr equilibrium fractionation in the aragonite-fluid system. The results of this study provide new insight into the mechanisms controlling stable Sr isotope composition in aragonite, which has implications for using Sr isotopes for paleo-reconstructions of natural archives, particularly those of abiogenic origin.

1. Introduction

Over the last two decades the number of proxies available to geochemists to reconstruct past environments has increased significantly owing to the development of increasingly accurate and sensitive analytical tools. Mass spectroscopic techniques allow measurements of the isotopic composition of major and trace metals in natural carbonate samples with high precision (e.g. Fietzke and Eisenhauer, 2006; Rüggeberg et al., 2008; Horner et al., 2015; Bates et al., 2017; Beinlich et al., 2018), and have opened numerous opportunities to interrogate sedimentary records. The demand for new proxy tools has led to a lot of experimental and theoretical work dedicated to understanding the physicochemical mechanisms that control the partitioning of metals and their isotopes between aqueous fluids and carbonate minerals. It is now acknowledged that, besides temperature, there are several parameters controlling the metal distribution coefficient and the isotope

* Corresponding author.
E-mail address: vasileios.mavromatis@unibe.ch (V. Mavromatis).
[1] Present address: Institute of Geological Sciences, University of Bern, Baltzerstr. 1+3, 3012 Bern, Switzerland.

https://doi.org/10.1016/j.gca.2023.08.013
Received 13 March 2023; Accepted 12 August 2023
Available online 15 August 2023

compositions in carbonate minerals. These include but are not limited to: the carbonate crystallography (Noireaux et al., 2015; Mavromatis et al., 2012; Harrison et al., 2021; 2023; Henehan et al., 2022), the mechanism and rate of growth (e.g. Boehm et al., 2012; Tang et al., 2008; Mavromatis et al., 2013; Mavromatis et al., 2020; Lammers et al., 2020; Mills et al., 2021), the bonding environment of the metal in the solid and its aqueous speciation (e.g. Schott et al., 2016; Mavromatis et al., 2019) as well as the fluid pH (e.g. Farmer et al., 2019; Mavromatis et al., 2021; Füger et al., 2019; Füger et al., 2022).

This study examines the Sr distribution and stable Sr isotope ($\Delta^{88/86}Sr$) fractionation between aragonite and fluid and reports first-principles calculations of Sr isotopes in this mineral-fluid system. Both aragonite ($CaCO_3$) and strontianite ($SrCO_3$) crystallize in the orthorhombic system where the metal (Ca, Sr) is coordinated to nine oxygens. The substitutions of Ca by Sr in aragonite whose ionic radii are equal to 1.18 and 1.31 Å, respectively (Shannon, 1976), leads to the formation of a regular solid-solution with a miscibility gap of $15 < \text{mol \% Sr} < 85$ at ambient conditions (Casey et al., 1996; Morse and MacKenzie, 1990). The presence of Sr in aragonite and the aragonite-strontianite solid-solution have been thoroughly studied for their mineralogic and crystallographic properties (Alia et al., 1997; Bucca et al., 2009; Casey et al., 1996; Kulik et al., 2010; Plummer and Busenberg, 1987; Plummer et al., 1992; Ruiz-Hernandez et al., 2010).

In geological systems the Sr partition coefficient between aragonite and the fluid is generally presumed to be equal to unity. This assumption is based on nucleation experiments (e.g. Dietzel et al., 2004; Gaetani and Cohen, 2006) in which the Sr/Ca ratios in the solid reflected that of the formation fluid, although the effect of mineral growth kinetics that has been shown to affect other traces in carbonate minerals (e.g. Voigt et al., 2017; Mavromatis et al., 2022) has not been thoroughly examined. The lack of difference in Sr/Ca ratios between fluid and solid is of great interest for environmental reconstructions as it suggests that aragonite growth kinetics should not affect elemental distribution. Therefore, Sr/Ca ratio in aragonite could be directly associated to other physico-chemical parameters. For instance, the Sr/Ca ratio in coralline aragonite samples has been shown to correlate with temperature, as evidenced by a linear relationship with respect to $\delta^{18}O$ compositions (Beck et al., 1992). However, this proxy tool has been questioned based on variations of Sr/Ca temperature relationships among different coral species (de Villiers et al., 1995; Marshall and McCulloch, 2002). The great interest in paleo-temperature estimation using a tool independent of $\delta^{18}O$ and the possible limitations it may have (e.g. fluid salinity; Schmidt, 1999) motivated the measurement of stable Sr isotope (i.e. $\delta^{88/86}Sr$) composition of aragonite in several studies. Early works (Fietzke and Eisenhauer, 2006; Rüggeberg et al., 2008) demonstrated temperature-dependent stable Sr isotope fractionation in coral skeletons. More recent studies (Raddatz et al., 2013; Fruchter et al., 2016), however, did not confirm these findings, but rather supported the use of $\delta^{88/86}Sr$ of the solid to reconstruct the stable Sr seawater composition. In a recent experimental study by AlKhatib and Eisenhauer (2017) where aragonite formed abiotically, temperature in the range 12.5–37.5 °C seemed to only have a weak effect on stable Sr isotope fractionation between aragonite and fluid. Interestingly, growth rate in this study was only observed to exert a minor effect on stable Sr isotope fractionation (AlKhatib and Eisenhauer, 2017), an observation that contradicts the strong isotope kinetic effects reported by Boehm et al. (2012) during Sr incorporation in calcite. Notably, however, in the study by AlKhatib and Eisenhauer (2017) Sr is present not only as a trace metal in aragonite, but mainly as strontianite ($SrCO_3$). The simultaneous formation of these two minerals in the experiments of AlKhatib and Eisenhauer (2017) makes the interpretation of their data ambiguous. To date, a clear application of stable Sr isotopes in aragonite as a paleo-proxy has not been adequately defined. A better mechanistic understanding of the fractionation of stable Sr isotopes during its incorporation into aragonite will inform development of this isotopic tool.

In the present study, co-precipitation experiments of Sr with aragonite have been conducted to evaluate the potential impact of growth kinetics on Sr distribution and stable isotope fractionation during its incorporation in this mineral phase. Additionally, the fractionation of stable Sr isotopes, together with those of C and O in the solid phase, have been estimated theoretically for Sr-rich aragonite and the aqueous phase. The experimental and theoretical results are compared and discussed in the light of Sr isotope fractionation during aragonite growth. The findings of this work suggest that mineral growth kinetics affect both the distribution and the stable isotope fractionation of Sr during aragonite growth and have implications for the interpretation of chemical and isotopic signatures in natural aragonites.

2. Methods

2.1. Precipitation experiments

Experiments of Sr co-precipitation with aragonite were performed on synthetic aragonite seeds at 25 °C and 1 bar pCO_2 using a mixed flow reactor setup following the protocol described earlier in Brazier and Mavromatis (2022). Synthesis of aragonite seeds followed the same protocol described in detail in Mavromatis et al. (2018). The seeds exhibited the needle-like structure that is typical for aragonite (Fig. 1A), contained ~80 μg/g Sr and had a specific surface area of 0.35 m^2/g (±10%). Aragonite growth was induced by the continuous pumping of two inlet solutions into the reactor, one containing $CaCl_2$, $MgCl_2$, and $SrCl_2$, and the second containing Na_2CO_3 and NaCl. The pumping rates of the two inlet solutions were quasi equal and controlled by a peristaltic pump supplying the reactors with 9.7–10.5 mL/24 h during all the runs of this study. The concentrations of Mg, Sr and Na in the inlet solutions were double compared to those present in the reactor in order to avoid changes in concentrations of the reactive fluid due to dilution. Note that Mg was used in the background electrolyte in order to avoid nucleation of calcite (Mavromatis et al., 2015). In all runs, the background electrolyte concentration was kept the same at 25 mM $MgCl_2$ and 250 mM NaCl. The inlet solutions contained various concentrations of $CaCl_2$ and Na_2CO_3 in the range of 70 to 300 mM allowing for variations in aragonite growth rate. All the solutions of this study were prepared using analytical grade chemicals and high purity deionized water. The pH of the reactive solution was controlled by the continuous bubbling of a water saturated CO_2 gas, which was bubbled in a 300 mM NaCl solution prior to its introduction into the reactor, in order to minimize evaporation. The continuous bubbling of CO_2 kept the pH constant at $\sim 6.3 \pm 0.1$ during the whole course of an experiment. Each reactor was equipped with a Teflon floating stir bar rotating at ~300 rpm. The introduction of the inlet solutions in the reactor resulted in an increase of the volume of the reactive solution, thus every 24 h, a volume of reactive fluid, equal to the sum of the volumes of the inlet solutions added in 24 h by the peristaltic pump, was sampled from the reactor to keep the volume within ±4%. Stirring was stopped shortly prior to sampling to allow the solid material to settle and thus minimize solid removal and keep the solid/fluid ratio quasi constant during the course of an experiment. After sampling, aqueous fluids were filtered through a 0.2 μm cellulose acetate membrane filter and a sub-sample was acidified for cation concentration and isotope analyses. Carbonate alkalinity and pH were determined in unacidified sub-samples. At the end of the experimental run, the entire reactive solution was vacuum filtered through a 0.2 μm membrane filter. The solids were rinsed with deionized water and dried at room temperature.

2.2. Chemical and mineralogical analyses

The concentrations of cations in reactive solutions were measured by Inductive Coupled Plasma Optical Emission Spectrometry (ICP-OES) using a PerkinElmer Optima (8300 DV) with an analytical precision of ±3% (2RSD) based on repeated analyses of NIST 1640a and seawater

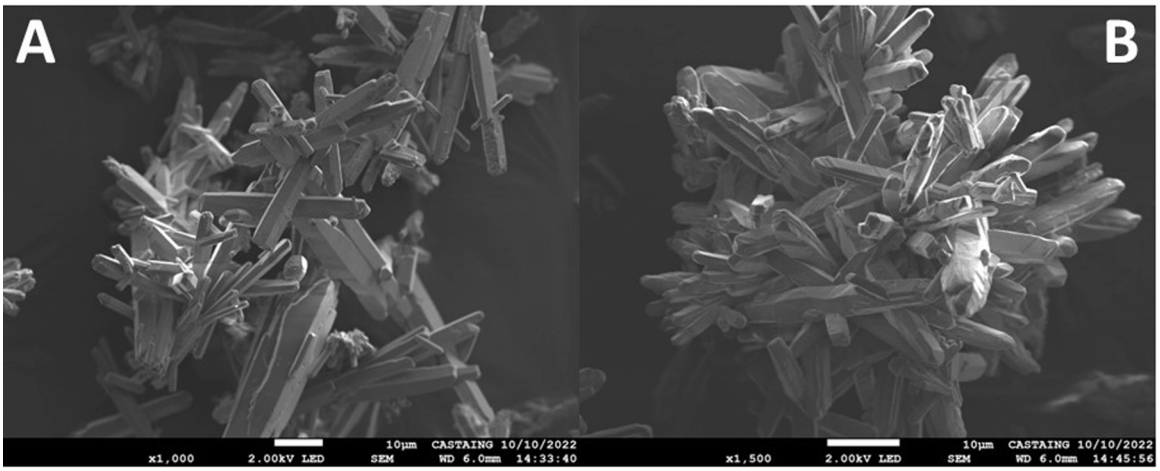

Fig. 1. Scanning Electron microphotographs of A) synthetic aragonite seed, and B) aragonite overgrowth collected from experiment ArSr3.

reference materials. Alkalinity was determined on a Schott TitroLine alpha plus titrator using a 10 mM HCl solution with an uncertainty of ±2%. The pH was measured with a Schott Blueline 28 combined electrode, calibrated with NIST standard buffers at pH of 4.01, 7.00 and 10.00 with an uncertainty of ±0.03 units. Aqueous speciation, ion activities and saturation states of the reactive fluids with respect to aragonite (i.e. $\Omega_{aragonite} = a_{Ca^{2+}} a_{CO_3^{2-}} / K_{sp,aragonite}$) were calculated using PHREEQC software together with its MINTEQ.V4 database (Parkhurst and Appelo, 2013) after the addition of the solubility products of hydromagnesite (Gautier et al., 2014) and nesquehonite (Harrison et al., 2019).

The mineralogy of the aragonite seeds and the solids recovered at the end of the experiments were assessed using their X-ray powder diffraction (XRD) patterns that were recorded on a PANalytical X'Pert PRO diffractometer using Co-Kα radiation (40 mA, 40 kV) at a 2θ range from 4° to 85° and a scan speed of 0.03° s^{-1}. Precipitates were carbon-coated and imaged using a JEOL JSM 7100F TTLS LV field emission scanning electron microscope (SEM). Specific surface area of the seed material and solids at the end of the experimental runs were determined by the BET technique (Brunauer et al., 1938) using krypton and 11 measured adsorption points. Chemical composition of the solids was defined after digestion of bulk precipitate using 2 N HNO_3 (Suprapur) and subsequent solution analysis by ICP-OES as described above.

2.3. Strontium isotope analyses

Stable Sr isotope analyses in this study were performed in GEOMAR (Kiel, Germany) and at the Cortecs-Pacite platform of the University of Strasbourg at ITES (Strasbourg, France). The analytical procedure followed in GEOMAR can be found in AlKhatib and Eisenhauer (2017). Briefly, for each sample, two fractions containing ~17.12 nmol of Sr were prepared. One fraction was mixed with a ^{84}Sr-^{87}Sr double spike for $\delta^{88/86}Sr$ analyses and the other was kept double spike free to measure the $^{87}Sr/^{86}Sr$ ratio. The samples were then purified by column chromatography using an Eichrom Sr-SPS resin (total blank procedure < 10^{-3} nmol), dried down and redissolved in 2 µL of H_3PO_4 before being loaded on a single rhenium filament covered with Ta_2O_5 activator. The detailed procedure followed at ITES is described in Brazier et al. (2020a). Briefly, for the $\delta^{88/86}Sr$ analyses, 4.62 nmol of Sr from each sample were mixed with 1.08 nmol of Sr from a ^{84}Sr - ^{87}Sr double spike, while for the $^{87}Sr/^{86}Sr$ analyses, 5.70 nmol of Sr from each sample was prepared and both dried down at 70 °C. The Sr was chemically separated from the matrix using a normal DGA resin (TODGA, Triskem™) following the protocol previously described in Brazier et al. (2019) allowing 100% of Sr recovery. After the complete elution of Sr, all the samples were dried down at 70 °C. The Sr blanks for the total chemical separation procedure represent less than 0.1% of the Sr loaded on the column and are considered negligible. The dried Sr residue were dissolved in 2–3 µL of 1 N HNO_3 and deposited on single rhenium filaments (99.98% purity) previously outgassed and covered with Ta_2O_5 activator.

The $\delta^{88/86}Sr$ measurements at GEOMAR and ITES were performed in static mode on a thermal ionization mass spectrometer (TIMS, Thermo Scientific Triton™) following the procedure of Krabbenhöft et al. (2009) and Brazier et al. (2020a). $\delta^{88/86}Sr$ are expressed as permil relative to the NIST SRM987 ($\delta^{88/86}Sr$ (‰) = $[(^{88}Sr/^{86}Sr)_{sample}/(^{88}Sr/^{86}Sr)_{standard}-1] *1000$) and the average reproducibility for the $\delta^{88/86}Sr$ measurements was calculated on all the samples measured in duplicates in this study. This method is based on the calculation of an associated variance to the average values of each sample and lead to a reproducibility of 0.11‰ (2SD, n = 20). Accuracy was ensured by repeated measurement of IAPSO (GEOMAR: 0.391 ± 0.004‰, n = 63; ITES: 0.381 ± 0.019‰, 2SD, n = 11). Lastly the accuracy and the intermediate precision of the $^{87}Sr/^{86}Sr$ measurements performed in ITES were assessed by repeated measurement of the NIST SRM987 at each measurement session (yielding a $^{87}Sr/^{86}Sr$ of 0.71025 ± 0.00002 (2SD, n = 25) over the last years and are consistent with previous measurements (Schmitt et al., 2017, Brazier et al., 2020a, 2020b).

2.4. First-principles calculations

The equilibrium fractionations of Sr, C, and O isotopes between minerals from the aragonite-strontianite solid-solution and aqueous Sr^{2+} were determined by first-principles calculations based on the density functional theory (DFT). Three crystal structures have been investigated: pure aragonite and strontianite ($CaCO_3$ and $SrCO_3$ respectively, *Pmcn* space group, orthorhombic unit cells), and one Sr-bearing aragonite ($Sr_{0.063}Ca_{0.937}CO_3$) obtained by substituting 1 Sr for Ca in a 2 × 1 × 2 aragonite supercell. Aqueous Sr^{2+} has been described using a cubic simulation cell containing 1 Sr atom and 64 water molecules. A uniform background charge has been applied to compensate for Sr^{2+} positive charge. The cell-parameter of the cubic box was set at 12.72 Å, so as to reproduce the experimental water density of 1000 kg/m^3 found at room-temperature.

According to Bigeleisen and Mayer (1947), the equilibrium isotopic fractionation factor (α) between two phases (*a* and *b*) can be determined from the reduced partition function ratios (*β*):

$$\alpha(a,b) = \beta(a)/\beta(b) \quad (1)$$

which can be more conveniently expressed in ‰ with the following logarithmic relation:

$$1000ln\alpha(a,b) = 1000ln\beta(a) - 1000ln\beta(b) \quad (2)$$

Since the equilibrium mass-dependent isotopic fractionation arises mainly from the change in vibrational energy induced by the isotopic substitution, the β -factor can be calculated from the harmonic vibrational frequencies as follows (e.g. Blanchard et al., 2017):

$$\beta = \left[\prod_{i=1}^{3N_{at}} \prod_{\{q\}} \frac{\nu^*_{q,i}}{\nu_{q,i}} \frac{e^{-h\nu^*_{q,i}/(2kT)}}{1-e^{-h\nu^*_{q,i}/(kT)}} \frac{1-e^{-h\nu_{q,i}/(kT)}}{e^{-h\nu_{q,i}/(2kT)}} \right]^{1/\left(nN_q\right)} \quad (3)$$

where $\nu_{q,i}$ and $\nu^*_{q,i}$ are the frequencies of the vibrational mode defined by indexes i ($i = 1,3N_{at}$) and wavevector q for the two isotopically distinct systems. N_{at}, N_q, n, h, k and T, *are* the total number of atoms in the simulation cell, the number of wavevectors, the number of isotopically exchanged sites, Planck's constant, Boltzmann's constant, and the temperature, respectively. The second product in Eq. (3) is performed on a sufficiently large grid of N_q wavevectors in the Brillouin zone.

For minerals, the structural relaxations (i.e. optimization of atomic positions and cell parameters) followed by the vibrational frequency calculations were performed using the PWscf and PHonon codes of the Quantum ESPRESSO package (Giannozzi et al., 2009; https://www.quantum-espresso.org). For aqueous strontium, DFT-based Born-Oppenheimer molecular dynamics simulations were carried out in order to ensure an acceptable sampling of Sr configurational disorder in solution. The simulation was performed in the NVT thermodynamic ensemble with the temperature fixed at 300 K and controlled by a Berendsen thermostat (Berendsen et al., 1984) with a coupling time constant of 0.3 ps. The time step used for the integration of equations of motion to evolve the ionic positions was 0.97 fs. More than 20 snapshots were regularly sampled along the 25 ps trajectory (after discarding the first 4 ps corresponding to the equilibration time) and Sr interatomic force constants were calculated within the density functional perturbation theory (DFPT or linear response theory). For aqueous strontium the same codes as for the minerals were used. In some cases, atomic positions of the snapshots were relaxed before calculating by DFPT the vibrational frequencies (at the center of the Brillouin zone) and Sr interatomic force constants, in order to establish and take advantage of the one-to-one relation between Sr β -factors and interatomic force constants as demonstrated by Ducher et al. (2016). As explained later in the results section, a second approach has consisted in optimizing both the box volume and the atomic positions of each snapshot at a target pressure of 0.0 ± 0.2 kbar before calculating the Sr interatomic force constant. All calculations used the generalized gradient approximation (GGA) to the exchange-correlation functional with the Perdew-Burke-Ernzerhof (PBE) parametrization (Perdew et al., 1996). The ionic cores of all elements were described by norm-conserving pseudopotentials from ONCV library (Schlipf and Gygi, 2015). The electronic wave functions and charge density were expanded using finite basis sets of plane-waves with 100 and 900 Ry cutoffs, respectively. In the case of minerals for which experimental Raman frequencies were available, it has been shown that using a larger cutoff (namely 140 Ry) improves the description of low-frequencies (<250 cm^{-1}) but has a very limited effect on β -factors (i.e. variation of 0.004‰ at 298 K, for strontianite $^{88/86}Sr$ β -factor which is equal to 1.181‰). Electronic integration is performed by sampling the Brillouin zone according to the Monkhorst-Pack scheme (Monkhorst and Pack, 1976). The size of the selected grids is shown in Table 1.

3. Results

3.1. Mineralogy and chemical composition of the precipitated solids

The X-ray diffraction patterns of the collected solids are indicative of aragonite with trace amounts of calcite and no sign of strontianite ($SrCO_3$) co-precipitation. This is consistent with the calculated values of the saturation state of the reactive fluids with respect to strontianite ($SrCO_3$) which remained undersaturated (i.e. $\Omega < 1$) in all experiments (Table 2). The solid materials recovered at the end of the experimental runs exhibit the same needle-like structure like the aragonite seed material (Fig. 1). The concentration of Sr in the overgrowths can be seen in Table 2 and ranged between 0.003 and 0.017 mol/mol Ca.

3.2. Chemical composition of the reactive fluids and growth rate calculations

The reactive fluids in the experimental runs achieve chemical steady state conditions with respect to aqueous Ca concentration within less than 1400 min from the onset of each run as it can be seen in Fig. 2 for experiment ArSr8. In contrast, aqueous Sr concentration decreases until it reaches chemical steady-state conditions typically after 7000 min from the onset of each run (Fig. 2). Under steady-state conditions, the growth rate of aragonite (r_p), expressed in mol/m^2/s, can be estimated based on mass balance considerations by taking into account the number of moles of Ca introduced in the reactor ($n_{Ca(add)}$) per unit time and the number of moles of Ca removed from the reactor via sampling along the same period of time ($n_{Ca(rem)}$) as:

$$r_p = \frac{n_{Ca(add)} - n_{Ca(rem)}}{86,400}/S \quad (4)$$

where S denotes the total surface area of aragonite in the reactor and is expressed in m^2 and 86,400 is the number of seconds in 24 h. The specific surface area of the aragonite overgrowths was within error (i.e. 10%) the same as that of aragonite seed (see Table 2). Thus, for growth rate calculation using Eq. (4), the surface area was estimated based on the total mass of aragonite (i.e. seed + overgrowth) present in the reactors at the end of the runs. Note that in this study the amount of Sr co-precipitated with aragonite has not been taken into consideration in rate calculation because it is negligible compared to that of Ca. As it can be seen in Table 2 the overall variation of growth rates in this study lays within the range $-8.4 \leq Logr_p \leq -7.7$ (mol/m^2/s). Note also that, as it can be seen in Fig. S1 of the supplementary material, increasing values of $\Omega_{aragonite}$, the saturation state of the solution with respect to aragonite, systematically lead to an increase of r_p values (Table 2).

Strontium apparent distribution coefficient between aragonite and the fluid under chemical steady state conditions can be expressed as (Henderson and Kracek, 1927)

$$D_{Sr,aragonite} = \frac{X_{SrCO_3}}{X_{CaCO_3}} \frac{[Ca]}{[Sr]} \quad (5)$$

where $[Sr]$ and $[Ca]$ stand for the molal concentrations of Sr and Ca in fluid, X_{SrCO_3} and X_{CaCO_3} refer to the mole fractions of $SrCO_3$ and $CaCO_3$ in aragonite overgrowths, respectively. Note that Eq. (5) makes use of total aqueous concentration of Sr and Ca and not of the concentrations of free ions. This approach has been chosen in this study because both these

Table 1
Computational parameters (k-point and q-point grids, "s" means "grid shifted with respect to the center of the Brillouin zone") and cell parameters and Sr—O average bond length (in Å) of mineral models. The DFT-optimized values are compared with experimental values in brackets (Antao and Hassan, 2009).

	Sr mol%	*k*-pts	*q*-pts	a	b	c	vol	Sr—O
Aragonite	0.0	4 × 3 × 4 s	3 × 2 × 2	5.006 (4.961)	8.023 (7.971)	5.810 (5.742)	233.35 (227.04)	–
Sr-Aragonite	6.3	2 × 3 × 2 s	1 × 1 × 1 s	5.016	8.049	5.834	235.52	2.633
Strontianite	100.0	4 × 3 × 4 s	3 × 2 × 2	5.154 (5.108)	8.482 (8.414)	6.136 (6.027)	268.24 (259.00)	2.681 (2.650)

Table 2
Strontium concentration of aragonite overgrowths and seed material, aqueous concentration of Ca and alkalinity, degrees of saturation of the fluid with respect to aragonite and strontianite, growth rate and Sr distribution in the aragonite for the experiments performed in this study. The values of factor A used in Eq. (9), together with the reactive surface area of the seed material and that of selected solids are reported.

Experiment	$Sr/Ca_{aragonite}$ (mol/mol)	Ca (mM)	Alkalinity (mM)	$\Omega_{aragonite}$	$\Omega_{strontianite}$	$Log r_p$ (mol/m^2/s)	$D_{Sr,aragonite}$	A	Surface area (m^2/g)
ArSr2	0.017	19.45	21.30	1.09	0.08	−8.4	2.55	0.50	
ArSr3	0.008	26.25	30.11	1.60	0.08	−7.9	1.61	0.51	0.29
ArSr4	0.004	38.48	26.00	1.75	0.07	−7.7	1.13	0.46	0.36
ArSr5	0.012	24.51	31.04	1.52	0.09	−8.3	2.13	0.50	
ArSr6	0.006	24.07	35.25	1.98	0.10	−7.7	1.28	0.50	0.29
ArSr8	0.015	24.76	26.42	1.59	0.10	−8.2	2.27	0.49	
ArSr9	0.007	28.04	26.71	1.76	0.08	−8.1	1.69	0.50	
ArSr10	0.003	39.49	23.95	2.23	0.07	−7.8	1.17	0.46	0.31
ArSr11	0.011	26.27	28.42	1.78	0.10	−8.1	1.89	0.50	
ArSr12	0.006	24.63	30.52	1.81	0.07	−7.8	1.54	0.50	0.23
seed	9.1×10^{-5}								0.35

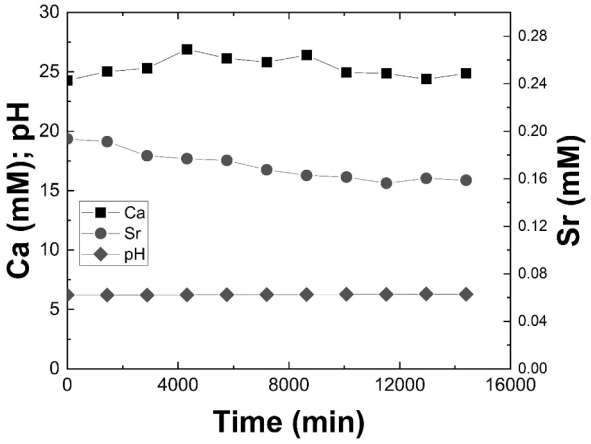

Fig. 2. Temporal evolution of aqueous Ca and Sr concentrations and pH in the reactive fluid in experiment ArSr8.

divalent cations occur in the free form (i.e. Me^{2+}) in the aqueous phase due to the low pH (i.e. ~6.3) prevailing during the experimental runs as it can be seen in Table S1. The estimated $D_{Sr,aragonite}$ values in the co-precipitation experiments of this study can be found in Table 2 and fall within the range $1.1 \leq D_{Sr,aragonite} \leq 2.6$. Additionally, as it can be seen in Fig. 3, the $D_{Sr,aragonite}$ values are systematically decreasing at

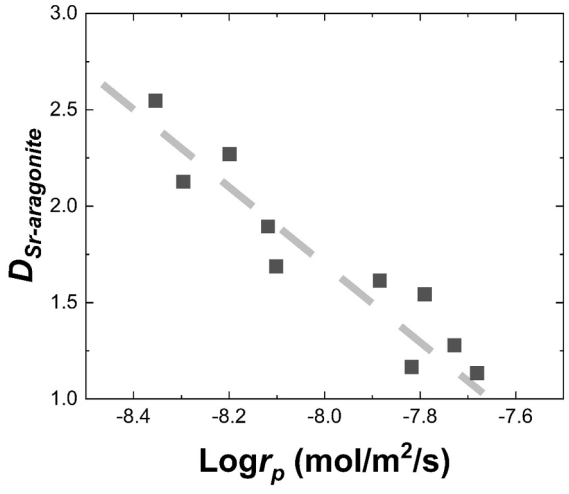

Fig. 3. Strontium distribution coefficient ($D_{Sr\text{-}aragonite}$) as a function of growth rate. The dashed line represents the linear fit that can be described with Eq. (6). Analytical uncertainties are included in the symbol size.

increasing growth rate. The dependence of $D_{Sr,aragonite}$ on growth rate can be described with the linear expression:

$$D_{Sr,aragonite} = -1.837(\pm 0.234) \times Log r_p - 12.963(\pm 1.876), \quad R^2 = 0.89 \qquad (6)$$

Moreover, a linear correlation between $D_{Sr\text{-}aragonite}$ and $\Omega_{aragonite}$ occurs as it can be seen in Fig. S1 that can be expressed as:

$$D_{Sr,aragonite} = -1.326\ (\pm 0.275) \times \Omega_{aragonite} + 4.030\ (\pm 0.485); R^2 = 0.74 \qquad (7)$$

which suggests that under chemical equilibrium conditions where $\Omega_{aragonite} = 1$, $D_{Sr,aragonite}$ reaches a value of ~2.7. Note that Eqs. (6) and (7) are valid for aragonite formed under the chemical conditions (e.g. pH≈6.3, $I = 0.3$ M) and for the growth rate ranges ($10^{-8.4} \leq r_p \leq 10^{-7.7}$ mol/m^2/s) explored in this study.

3.3. Strontium isotope composition of reactive fluids and solids

The $\delta^{88/86}Sr$ compositions of the selected reactive fluids and solids can be seen in Table 3. Compared to the stock $SrCl_2$ solution, the reactive fluids collected at the end of the runs exhibit higher $\delta^{88/86}Sr$ values, reflecting an enrichment in the heavier ^{88}Sr. Interestingly, as it can be seen in Fig. 4A, within an experimental run the $\delta^{88/86}Sr_{fluid}$ values increased over time until achievement of isotopic steady state after ~8000 min (Table 3). This observed enrichment in ^{88}Sr of the reactive fluid suggests a depletion of the precipitating aragonite in ^{88}Sr isotope. Indeed, as it can be seen in Table 3, all the $\delta^{88/86}Sr_{solid}$ values are systematically lower than that of the $SrCl_2$ stock solution.

The apparent isotope fractionation between aragonite and reactive fluid can be calculated using the expression:

$$\Delta^{88/86}Sr^*_{aragonite-fluid} = \delta^{88/86}Sr_{solid} - \delta^{88/86}Sr_{fluid} \qquad (8)$$

and, as it can be seen in Table 3, it spans within the range $-0.13‰ \leq \Delta^{88/86}Sr^*_{aragonite-fluid} \leq -0.32‰$. The $\Delta^{88/86}Sr^*_{aragonite-fluid}$ exhibits a rather weak dependence on growth rate with the smallest fractionation of −0.13‰ occurring at the lowest growth rate ($10^{-8.4}$ mol/m^2/s) in experimental run ArSr2, and the largest fractionation of −0.32‰ occurring at the highest growth rate ($10^{-7.7}$ mol/m^2/s) in experimental run ArSr6.

The temporal increase of the $\delta^{88/86}Sr_{fluid}$ (Fig. 4A), likely results in the growth of isotopically zoned aragonite crystals. As such the $\delta^{88/86}Sr_{solid}$ values of the bulk aragonite collected at the end of the runs cannot be used to estimate fractionation factors with the aid of Eq. (8). In order to avoid such artifacts, the isotopic fractionation between formed aragonite and reactive fluid under isotopic steady state conditions has been calculated based on mass-balance considerations using the equation:

Table 3
Strontium $\delta^{88/86}Sr$ composition of fluid and solid samples and reference materials measured in this study. The Sr solid–fluid fractionation factors are reported based on Eqs. (8) and (9). Uncertainties of fractionation factors have been estimates as the square root of the sum of the squares of the uncertainties of fluid and solid analyses. The second number appearing after the experiment in the column "sample" refers to the sampling point during the runs.

Sample	Fluids $\delta^{88/86}Sr$ (‰)	2σ	Sampling time (min)	Solids $\delta^{88/86}Sr$ (‰)	2σ	$\Delta^{88/86}Sr^{*}_{aragonite-fluid}$ (‰)	2σ	$\Delta^{88/86}Sr_{aragonite-fluid}$ (‰)	2σ
ArSr2-10	0.226	0.009	14,400	0.076	0.009	−0.150	0.013	−0.13	0.013
ArSr3-10	0.283	0.017	14,400	0.048	0.009	−0.235	0.019	−0.24	0.019
ArSr4-1	0.161	0.009	1440						
ArSr4-6	0.277	0.005	8640						
ArSr4-10	0.267	0.009	14,400	0.001	0.008	−0.266	0.012	−0.40	0.012
ArSr5-10	0.208	0.016	14,400	−0.069	0.010	−0.277	0.018	−0.10	0.018
ArSr6-1	0.195	0.006	1440						
ArSr6-6	0.315	0.019	8640						
ArSr6-10	0.357	0.035	14,400	0.036	0.009	−0.321	0.036	−0.38	0.036
ArSr8-10	0.205	0.008	14,400	0.076	0.010	−0.130	0.013	−0.13	0.013
ArSr9-10	0.203	0.009	14,400					−0.06	
ArSr10-1	0.167	0.019	1440						
ArSr10-6	0.234	0.022	8640						
ArSr10-10	0.241	0.010	14,400	−0.043	0.009	−0.284	0.013	−0.15	0.013
ArSr11-10	0.212	0.008	14,400	−0.033	0.009	−0.244	0.012	−0.12	0.012
ArSr12-10	0.339	0.016	14,400	0.070	0.014	−0.269	0.021	−0.28	0.021
IAPSO	0.399	0.004							
Sr-stock (Kiel)	0.173	0.013							
Sr-stock (Strasbourg)	0.174	0.009							

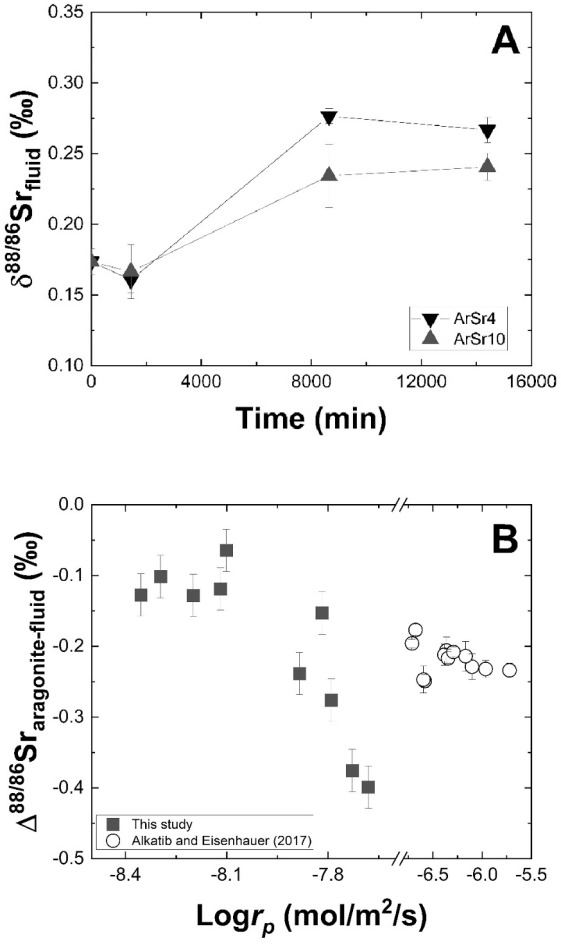

Fig. 4. (A) Temporal evolution of $\delta^{88/86}Sr_{fluid}$ in experiments ArSr4 and ArSr10 and (B) $\Delta^{88/86}Sr_{aragonite-fluid}$ estimated with the aid of Eq. (9) as a function of growth rate together with data by AlKhatib and Eisenhauer, (2017).

$$\Delta^{88/86}Sr_{aragonite-fluid} = \frac{1}{1-\frac{[Sr_{fluid}]}{A\times[Sr_{inlet}]}}\left(\delta^{88/86}Sr_{inlet} - \delta^{88/86}Sr_{fluid}\right) \quad (9)$$

where $[Sr_{fluid}]$ and $[Sr_{inlet}]$ refer to the concentration of Sr in the reactive fluid under isotopic steady-state conditions and to that of the inlet, respectively, $\delta^{88/86}Sr_{inlet}$ and $\delta^{88/86}Sr_{fluid}$ denote the isotopic composition of the inlet and the reactive fluid at isotopic steady-state, respectively, and A is a factor correcting the Sr concentration, considering that small variation in the proportions of the two inlet solutions among the runs may have occurred (see Mavromatis et al., 2019). The values of factor A for the runs of this study can be found in Table 2. The estimated $\Delta^{88/86}Sr_{aragonite-fluid}$ values calculated with Eq. (9), that can be seen in Table 3 and Fig. 4B, exhibit small differences compared to those estimated with Eq. (8) and lay within the range $-0.06‰ \leq \Delta^{88/86}Sr_{aragonite-fluid} \leq -0.40‰$. Notably, as it can be seen in Fig. 4B, the $\Delta^{88/86}Sr_{aragonite-fluid}$ averages at $-0.1 \pm 0.05‰$ at $r_p \leq 10^{-8.2}$ (mol/m²/s). When $r_p \geq 10^{-8.0}$ (mol/m²/s), the $\Delta^{88/86}Sr_{aragonite-fluid}$ values exhibit a systematic decrease towards larger fractionation factors.

3.4. Structural, vibrational and isotopic properties of minerals from DFT

DFT-optimized cell parameters of minerals are slightly larger than their experimental counterparts (Table 1). The unit cell volume of aragonite and strontianite are respectively +2.8% and +3.6% larger than the experimental values reported in Antao and Hassan (2009), and the Sr—O average bond length of strontianite is 1.15% larger than the experimental one. The relative increase of the three orthorhombic cell parameters (i.e. *a*, *b* and *c*) along the $CaCO_3$-$SrCO_3$ solid solution is well-reproduced in the conducted calculations (Fig. S2), which suggests that the Sr-bearing aragonite models are fairly reliable. Since the prediction of the equilibrium isotopic fractionation relies on the good quality of vibrational frequencies (Eq. (3), calculated Raman frequencies are compared with the available experimental frequencies (Fig. S3 and Table S2). Both aragonite and strontianite display calculated Raman frequencies that are slightly smaller than the values measured by Lin and Liu (1997), with an average underestimation of about 3%. Such an accuracy on the structural and vibrational properties is typical of the current theoretical approach (DFT with GGA-PBE functional), and the similar response of $CaCO_3$ and $SrCO_3$ structures suggests that fractionations within the solid solution will be even more accurate through error cancellation. The reduced partition function ratios (β -factors) for C, O

and Sr isotopes were determined from the calculated vibrational frequencies using Eq. (3) and the polynomial fits of their temperature dependence are reported in Table 4. Looking at the C or O isotope fractionation between minerals of the $Sr_xCa_{1-x}CO_3$ solid-solution and $CaCO_3$ aragonite, a progressive increase of the fractionation with the Sr content in aragonite can be observed denoting that Sr-bearing aragonite being lighter than pure aragonite (Fig. 5). These DFT-based trends display similar slopes as the trend obtained from Raman and infrared frequencies measured on samples synthesized at $P = 1.5$ GPa and $T = 1300$ °C (Wang et al., 2021). However, the solid solution is only complete at a temperature above 400 K according to Wang et al. (2021).

3.5. Structural and isotopic properties of aqueous Sr^{2+} from DFT

Analysis of the ~25 ps long molecular dynamics trajectory indicates that the Sr^{2+} cation is surrounded on average by 7.05 water molecules in the first solvation shell, with an average Sr—O distance of 2.59 Å (Fig. S4). For comparison, the structural investigation of aqueous Sr^{2+} ion performed by Moreau et al. (2002) based on X-ray absorption spectroscopy determined an average Sr—O distance of 2.60 Å and a coordination number of 8.0 ± 0.3, while literature data show a range of coordination number between 7.3 and 10.3 depending on the method employed (XAFS, neutron or X-ray diffraction, molecular dynamics simulations; Moreau et al. 2002 and references therein).

From this molecular dynamics trajectory, the conventional approach to find the Sr β -factor is to sample several snapshots regularly spaced in time, to relax their atomic positions before computing the vibrational frequencies that are needed to apply Eq. (3). This structural relaxation step approach prevents negative or "imaginary" frequencies. This approach has been applied on several snapshots and also allowed to establish the one-to-one relation between Sr β -factors and Sr interatomic force constants (i.e. F_{Sr}) at different temperatures ranging from 273 K to 473 K (Fig. S5). As demonstrated by Ducher et al. (2016), this relation has several advantages: (i) computing the F_{Sr} is less demanding in computational resources than computing the whole phonon frequencies, (ii) it is possible to dispense with the snapshot relaxation step and calculate the force constants directly allowing to retain the full configurational disorder of the liquid. It is noteworthy that Bigeleisen and Mayer (1947) also derived a series of approximate formulae, including one relating directly the β -factor to the mean interatomic force constant (F):

$$\beta = 1 + \frac{m - m'}{mm'} \frac{\hbar^2 F}{8(kT)^2} \quad (10)$$

where $\hbar = h/2\pi$, m and m' are the atomic masses of the two isotopes. However, as shown in Fig. S6, the use of this approximate formula leads to a deviation of the Sr β -factor that increases toward lower temperatures. This explains why instead of Eq. (10), the linear correlations of Fig. S5, established from full frequency calculations (Eq. (3), were used.

Thus, Fig. 6A shows the interatomic force constant of aqueous Sr^{2+} calculated from the unrelaxed snapshots. The scattering of the snapshot values reflects the dynamic behavior of the liquid system, but the average force constant is fairly constant after about ten snapshots, leading to the value of 0.137 ± 0.016 Ry/au^2. From this force constant and the linear correlations shown in Fig. S5, the temperature dependence of aqueous Sr^{2+} was defined and its equation is reported in Table 5.

The aim of this work is to combine β -factors from minerals and the aqueous ion to provide the theoretical equilibrium isotopic fractionation between the solid and the liquid phase. In this case, it is important that both phases are treated as consistently as possible. As the minerals were modeled at their equilibrium volume for a pressure of 0.0 kbar, we tested here for aqueous Sr^{2+} to optimize both the box volume and the atomic positions of each snapshot at a target pressure of 0.0 ± 0.2 kbar before calculating the Sr interatomic force constant. Results are shown in Fig. 6B. As the atomic positions are now optimized, part of the disorder is erased and data are less scattered. Following this approach, the average force constant is found to be a bit larger, i.e. 0.151 ± 0.006 Ry/au^2, and the corresponding temperature dependence of Sr β -factor is also given on Table 5. It is interesting to note that the relaxation does not change significantly the average Sr—O distance (2.63 Å and 2.60 Å, before and after relaxation) and Sr coordination number (7.0 and 7.1, before and after relaxation).

3.6. Strontium isotope fractionation between minerals and aqueous Sr^{2+} from DFT

Combination of the minerals Sr β -factors (Table 4) and aqueous Sr^{2+} β -factors (Table 5) enables to derive the temperature dependence of the mineral-solution isotopic fractionation (Fig. 7) or the isotopic fractionation as a function of the mineral Sr content at a given temperature (Fig. 8). Results are shifted depending on the selected Sr^{2+} β -factor. Relaxing the volume of the water simulation box lowers the curves (Fig. 7) and leads to negative mineral-solution fractionations.

4. Discussion

4.1. Distribution of Sr between aragonite and fluid

Previous studies have documented a linear correlation between Sr/Ca ratios and $\delta^{18}O$ compositions of aragonite in corals, suggesting a relationship exists between temperature and Sr/Ca ratio (Beck et al., 1992). Conditions under which this relationship is valid will depend on the precipitation pathway (e.g., abiogenic vs. biogenic), and the impact of parameters other than temperature on Sr incorporation. In this study, the impact of growth rate on Sr incorporation was examined and it was observed that the $D_{Sr,aragonite}$ value is not always equal to 1 as previously assumed. As can be seen in Fig. 3, the value of the apparent distribution coefficient measured in this study at the lowest aragonite growth rate (exp. ArSr2 with $r_p = 10^{-8.4}$ mol/m^2/s) is 2.55. The decrease of D_{Me} with increasing mineral precipitation rate has similarly been observed for the incorporation of Co^{2+}, Fe^{2+}, Mn^{2+} and Ni^{2+} in calcite (Dromgoole and Walter, 1990; Lakshtanov and Stipp, 2007; Lee and Reeder, 2006; Castillo-Alvarez et al., 2021). The decrease in D_{Me} with increasing growth rate reflects the tendency of the Me/Ca ratio in the solid to approach that in the fluid at higher precipitation rates ($D_{Sr,aragonite} = 1$). Note however, that although at far from equilibrium conditions the Me/Ca ratio in the growing $CaCO_3$ phase can approach that in the fluid, under near equilibrium conditions thermodynamics control elemental distribution. Indeed during mineral growth at $\Omega_{MeCO3} \approx 1$ the elemental distribution of Me^{2+}, or in other words the preferred Me^{2+} affinity for the solid or the fluid, is controlled by the structural parameters in the two phases. As such Cd^{2+}, Co^{2+}, and Ni^{2+}, that coordinate to six oxygens both in calcite and the fluid phase, and obtain ionic radii close to that of calcium in calcite, exhibit a preferential affinity for the solid under near equilibrium conditions ($D_{Me,calcite} > 1$; Lorens, 1981; Lee and Reeder, 2006; Castillo-Alvarez et al., 2021). In contrast, during the

Table 4
Polynomial fits of type $ax^3 + bx^2 + cx$ of $10^3 \ln \beta$, with $x = 10^6/T^2$ (T in K) for C, O and Sr isotopes.

	Sr (mol %)	Isotope ratio	a	b	c
Aragonite	0.0	$^{13/12}C$	0.024423	−0.925575	23.191064
		$^{18/16}O$	0.007210	−0.307958	10.802106
Sr-Aragonite	6.3	$^{13/12}C$	0.024423	−0.925559	23.188480
		$^{18/16}O$	0.007212	−0.308012	10.798606
		$^{88/86}Sr$	–	−0.000277	0.130484
Strontianite	100.0	$^{13/12}C$	0.023541	−0.898432	22.787719
		$^{18/16}O$	0.006903	−0.297499	10.580153
		$^{88/86}Sr$	–	−0.000207	0.107219

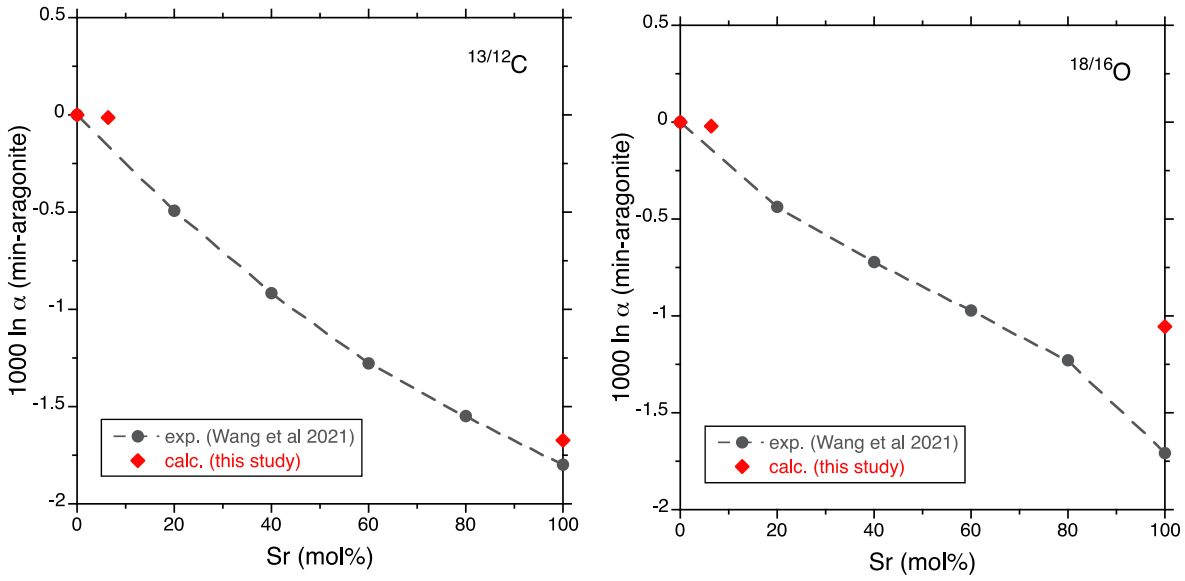

Fig. 5. Carbon (left) and oxygen (right) isotope fractionation factors between minerals of the $Sr_xCa_{1-x}CO_3$ solid-solution and $CaCO_3$ aragonite as a function of Sr content (in mol%) plotted at the temperature of 400 K at which the miscibility gap in the solid-solution disappears (Wang et al., 2021). Values calculated in this study are compared with the results of Wang et al. (2021), where the reduced partition function ratios (β -factors) were obtained from the Raman and infrared frequencies measured on synthetic samples.

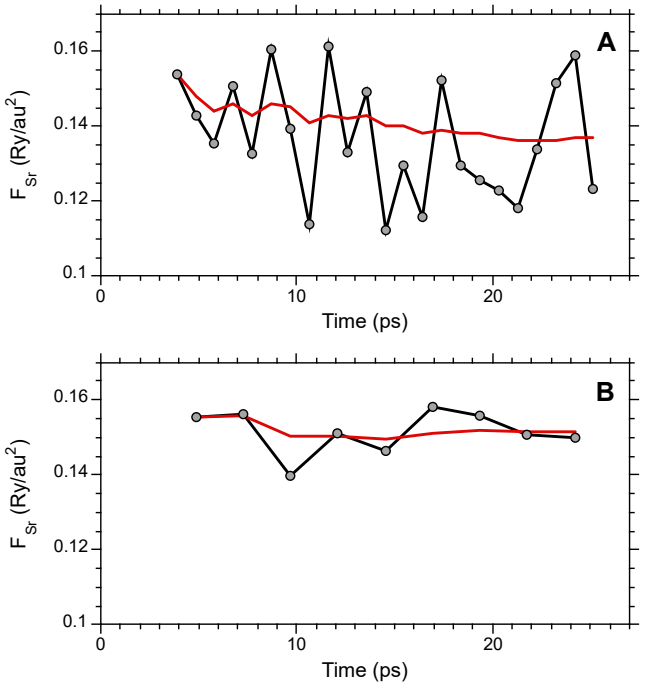

Fig. 6. Interatomic force constant of aqueous Sr^{2+} (in Ry/au^2) calculated from regularly sampled snapshots along the molecular dynamics trajectory (black circles) and its cumulative average (red curve). A) Volume of the simulation box fixed to a density of 1000 kg/m^3. Atomic positions in the snapshots were not relaxed. B) The volume of the simulation box and the atomic positions were relaxed at a target pressure of 0.0 ± 0.2 kbar before calculating the force constants.

incorporation of Co^{2+} and Ni^{2+} in aragonite, the coordination of these ions must increase from 6 to 9 which leads to a significant increase of the Me-O bond length. Therefore the value of $D_{Me,aragonite}$ is ≪1 at equilibrium and tends to increase rather than decrease with growth rate (Brazier and Mavromatis, 2022).

Strontium exhibits comparable coordination and Sr—O bond length

Table 5
Temperature dependence (0–200 °C) of aqueous Sr^{2+} β -factor based on the polynomial fit of type $ax^2 + bx + c$ of $10^3 \ln \beta$, with $x = 10^6/T^2$ (T in K) for $^{88/86}Sr$ isotopic ratio.

	a	*b*	*c*
Volume fixed for d = 1000 kg.m^{-3}	−0.000332	0.119638	0.003918
Volume optimized at P = 0.0 ± 0.2 kbar	−0.000366	0.134308	0.004115

in the fluid and aragonite and presents an equilibrium $D_{Sr,aragonite} > 1$ that decreases towards 1 with increasing growth rate. Similar growth rate dependence of $D_{Sr,aragonite}$ has been observed by DeCarlo et al. (2015), although the overall variation in $D_{Sr,aragonite}$ reported by these authors is significantly smaller compared to that measured in the present study (Fig. S7). Notably, the $D_{Sr,aragonite}$ value of 2.5 determined in this study for an aragonite growth rate of $10^{-8.4}$ mol/m^2/s is to our knowledge the largest reported in the literature. Earlier works reported $D_{Sr,aragonite}$ values around 1 and specifically 0.98 (n = 19) at 25 °C and various salinities (Zhong and Mucci, 1989), 1.23 (n = 4) at 19 °C (Dietzel et al., 2004), 1.13 at 25 °C (Gaetani and Cohen, 2006) and 1.11 (n = 21) at 25.5 °C (DeCarlo et al., 2015). Likely these lower values of Sr distribution coefficients compared to the present study could be assigned to aragonite formation at significantly faster growth rates, formation solution composition and pH. For example, in the study by DeCarlo et al. (2015), small variations in $D_{Sr,aragonite}$ values correlate well with growth rate ($R^2 = 0.8$) for all experiments performed at pH > 8.2 (see Fig. S7). At lower pH values however a large scatter in the data occurs, which may reflect changes in the mechanism of mineral formation (Morse, 1983). Additionally, it should be considered that the presence of anions in the forming fluid and solid can affect elemental distribution (e.g. Goetschl et al., 2019; Uchikawa et al., 2023). As such the higher $D_{Sr,aragonite}$ values of this study compared to those of Zhong and Mucci (1989) who conducted experiments in solutions characterized by $\Omega_{aragonite} < 2$ at pH≈8.0 but used seawater with different salinities may be attributable to differences in anion compositions in the fluid.

The thermodynamics of solid-solutions (i.e. Saxena, 1973) allows to define Sr thermodynamic distribution coefficient as the equilibrium constant of the Ca-Sr exchange reaction between aragonite and

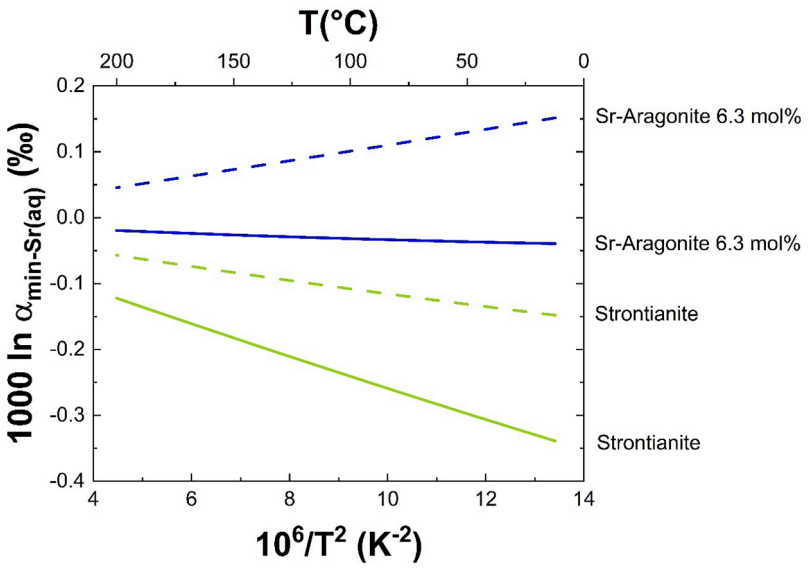

Fig. 7. Temperature dependence of the equilibrium fractionation factor between minerals and aqueous Sr^{2+}, calculated using either the molecular dynamics trajectory run at a density of 1000 kg/m^3 (dashed curves) or the snapshots relaxed at a target pressure of 0.0 ± 0.2 kbar (solid curves). The latter approach is more consistent with the modeling of the minerals.

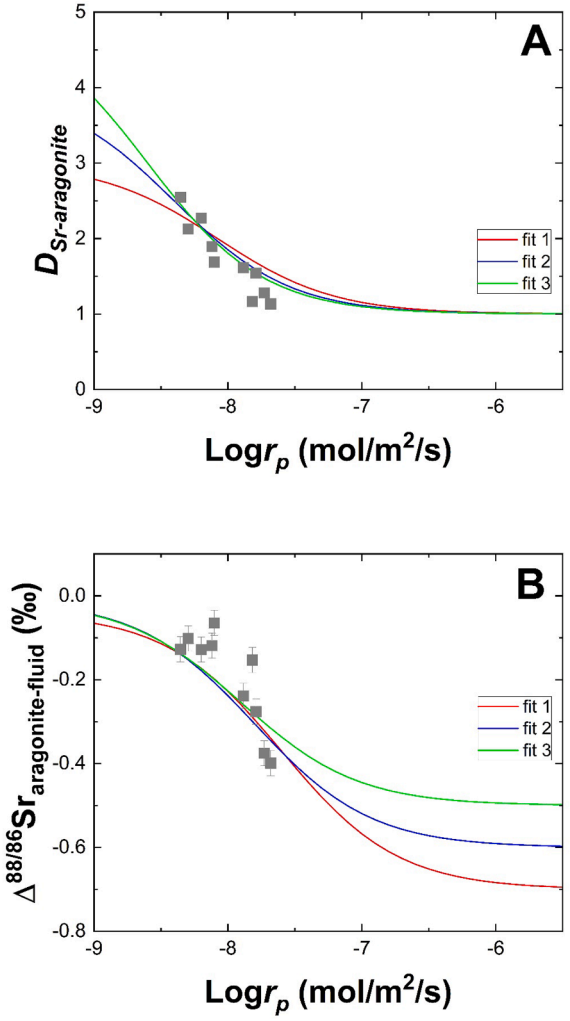

Fig. 8. Best-fit line of the SRK model to the experimental data of A) $D_{Sr,aragonite}$ and B) $\Delta^{88/86}Sr_{aragonite\text{-}fluid}$ using Eqs. (13) and (14), respectively. The parameters used for the fits can be found in Table 6.

strontianite:

$$CaCO_3(ss) + Sr^{2+} = SrCO_3(ss) + Ca^{2+},$$
$$D^*_{Sr,aragonite} = \frac{X_{SrCO_3}(ss)\gamma_{SrCO_3}(ss)\alpha_{Ca^{2+}}}{X_{CaCO_3}(ss)\gamma_{CaCO_3}(ss)\alpha_{Sr^{2+}}} \quad (11)$$

where X_i and γ_i represent the mole fraction and activity coefficient, respectively, of the i^{th} solid component of the solid solution, and a_i denotes the activity coefficient of the i^{th} aqueous ion. At equilibrium, the two constituents of the solid solution, $SrCO_3$(ss) and $CaCO_3$(ss), should be simultaneously in equilibrium with the two end-members of the solid-solution, which provides two additional relations involving the strontianite and aragonite solubility products:

$$K_{aragonite} = \frac{a_{Ca^{2+}}a_{CO_3^{2-}}}{X_{CaCO3}\gamma_{CaCO3}} \quad (12)$$

and

$$K_{strontianite} = \frac{a_{Sr^{2+}}a_{CO_3^{2-}}}{X_{SrCO3}\gamma_{SrCO3}} \quad (13)$$

Combination of Eqs. (11), (12) and (13) leads to the following expression for Sr thermodynamic partition coefficient:

$$D^*_{Sr,\ aragonite} = \frac{K_{aragonite}}{K_{strontianite}} \quad (14)$$

Considering that at 25 °C the solubility product of aragonite is equal to $10^{-8.34}$ (Plummer and Busenberg, 1982) and that of strontianite is equal to $10^{-9.27}$ (Busenberg et al., 1984), a $D^*_{Sr,aragonite}$ value of 8.5 can be derived. For the diluted solid solutions investigated in the present study $\gamma_{CaCO_3(ss)} \rightarrow 1$ and $\gamma_{SrCO_3(ss)} \rightarrow$ constant ($\lambda \neq 1$) whereas both aqueous Ca and Sr occur at the pH of 6.3 in the experimental solutions as Me^{2+} free ions with the same activity coefficients. This leads to $\frac{D^*_{Sr,aragonite}}{D_{Sr,aragonite}} = \lambda$ with a plausible λ value of 3 derived from the equilibrium Sr apparent distribution coefficient, $D_{Sr,aragonite} = 2.7$, obtained by extrapolation of the data of the present study at $\Omega_{aragonite} = 1$ with the aid of Eq (7). These observations confirm that under slow growth rates Sr would preferentially be incorporated in aragonite as implied by structural considerations and shown at the low aragonite growth rates of this study. At increasing growth rate, however, the forming solid would approach the

composition of the fluid yielding $D_{Sr,aragonite}$ values of ~1.

The growth-rate dependence of $D_{Sr,aragonite}$ values depicted in Fig. 3 reflects aragonite formation from solutions where $\Omega_{aragonite} \leq 2.2$ (Table 2; Fig. S1). It does not apply to oceanic waters where $\Omega_{aragonite} \geq 4.7$ (Feely et al., 2009) but rather to aragonite formation under small degrees of oversaturation such as those met during the formation of speleothems. Although aragonite is not commonly forming in cave environments where the predominant $CaCO_3$ phase is the thermodynamically more stable calcite, the recent work by Wassenburg et al. (2016) reported an enrichment of aragonite in Sr and a $D_{Sr,aragonite}$ value of ~2.4 at the lowest estimated speleothem extension rate, but a progressive decrease of this value to ~1 at increasing speleothem extension rates. This observation suggests that the relationship of $D_{Sr,aragonite}$ with growth rate and the degree of fluid supersaturation with respect to aragonite that are described with the aid of Eqs. (6) and (7) can be used as speleothem aragonite growth proxy after proper calibration for background solution composition and temperature. On the other hand, the formation of aragonite at higher growth rates suggests that the commonly used $D_{Sr,aragonite} = 1$, makes this archive suitable as proxy of past environmental parameters such as Sr/Ca of seawater or aragonite formation temperature. Whether $D_{Sr,aragonite}$ can be used as a growth proxy in aragonitic hard parts of calcifiers or not, cannot be assessed solely on the findings of this study. The biomineralization processes occurring during calcification commonly proceed at elevated degrees of saturation of the biomineralizing fluid with respect to $CaCO_3$ phases compared to seawater conditions (DeCarlo et al., 2017; Farfan et al., 2018) and in the presence of organic molecules (e.g. enzymes) that can modify Sr/Ca of the mineralizing fluid compared to seawater via formation for example of Ca^{2+}-ATPase (Cohen and McConnaughey, 2003). It remains unclear how these biogenic processes affect the Sr distribution, yet earlier works showed various correlation between Sr/Ca ratio and growth rate in bioprecipitated aragonite. For example, Sr/Ca ratio is inversely correlated to extension rates in corals (de Villiers et al., 1995; Ferrier-Pages et al., 2002), however a positive correlation is observed in some clam species (Gillikin et al., 2005), whereas no correlation has been observed in *A. islandica* bivalves (Foster et al., 2009). It has to be emphasized, however, that caution is required in the interpretation of Sr/Ca in aragonitic samples with respect to the presence of Sr in the solid that may occur either as a trace element randomly distributed in the solid or as a pure mineral phase domain (i.e. $SrCO_3$). Based on synchrotron techniques (i.e. XANES and EXAFS), Sr has been shown for example to randomly substitute for Ca in *A. Islandica* aragonitic shells (e.g. Foster et al., 2009), while both random substitution for Ca (e.g. Finch and Allison, 2003) and $SrCO_3$ domains (Greegor et al., 1997) have been observed in corals. The physicochemical parameters controlling the presence of Sr either as an impurity in aragonite or as $SrCO_3$ domains are not necessarily the same and may affect the interpretations of Sr/Ca ratio in aragonite and its use as growth rate or temperature proxy.

4.2. Equilibrium stable Sr isotope fractionation between aragonite and fluid

Under equilibrium conditions the results of first-principles calculations yield an equilibrium Sr isotope fractionation factor of −0.04‰ which is in excellent agreement with the experimental $\Delta^{88/86}Sr_{aragonite\text{-}fluid}$ value of −0.1 ± 0.05‰ measured at aragonite growth rates $r_p \leq 10^{-8.0\pm0.2}$ (mol/m^2/s) and $\Omega_{aragonite} \leq 1.5$ in the present study. Notably the lack of significant fractionation during Sr incorporation in aragonite contrasts that reported recently for Ca isotopes in the same mineral phase by Harrison et al. (2023) where $\Delta^{44/40}Ca_{aragonite\text{-}Ca2+} \approx$-1.6‰. This difference can be assigned to the significant increase of the mean Ca-O bond length following Ca^{2+} incorporation in aragonite from 2.41 Å in the Ca^{2+}(aq) ion (Ikeda et al., 2007; Bogatko et al., 2013) to 2.53 Å in aragonite (Speer, 1983). In contrast, Sr^{2+} incorporation into aragonite lattice proceeds without a significant increase of the mean Sr—O bond length (2.60 vs 2.63 Å, this study). As such Sr isotope fractionation between solid and fluid is significantly smaller.

4.3. Quantification within the framework of the surface reaction kinetic model (SRKM) of the impact of growth kinetics on $D_{Sr,aragonite}$ and $\Delta^{88/86}Sr_{aragonite\text{-}fluid}$

Under the relatively small fluid supersaturations of the present study ($\Omega_{aragonite} \leq 2.2$), aragonite growth follows a standard growth mechanism involving ion-by-ion attachment to advancing steps. Within such a mechanism, it can be expected that desolvation of aqueous Sr and subsequently the rate of exchange of water molecules in its coordination sphere control the incorporation of this metal in carbonate crystal lattice (Pokrovsky and Schott, 2002; Schott et al., 2009; Hofmann et al., 2012). According to Hofmann et al. (2012) the exchange rate of water between the metal hydration sphere and the bulk fluid follows an inverse power-law mass dependence. Thus, the lighter isotopes are preferentially incorporated into the growing mineral and the associated kinetic isotope fractionation should increase at elevated mineral growth rate.

The impact of aragonite growth kinetics on the extent of $D_{Sr,aragonite}$ and $\Delta^{88/86}Sr_{aragonite\text{-}fluid}$ could be quantified by the surface reaction kinetic model (SRKM) developed by DePaolo (2011). This model has been earlier applied to successfully describe the chemical distribution and stable isotope fractionation of major and trace metal cations (e.g. Ba, Ca, Li, Mg, Sr) in carbonate minerals such as calcite, aragonite and magnesite (e.g. DePaolo, 2011; Nielsen et al., 2012; Pearce et al., 2012; Lammers et al., 2020; Mavromatis et al., 2020; Füger et al., 2022). The SRKM makes use of equations for the forward (precipitation, R_f) and backward (dissolution R_b) reaction for the two members of elemental (i.e. $CaCO_3$[s]) and $SrCO_3$[s]) or isotopic (i.e. Ca,$^{88}SrCO_3$ [ss] and Ca,$^{86}SrCO_3$ [ss]) solid solutions, implying that two kinetic factors are associated with the forward and backward reaction. Assuming a first order dependence of $CaCO_3$ growth rate on the fluid saturation state, DePaolo (2011) derived the following expression for *Dss* under steady state growth conditions:

$$D_{SS} = \frac{D_f}{1 + \frac{R_b}{R_{net}+R_b}\left(\frac{D_f}{D_{eq}} - 1\right)} \quad (15)$$

where D_{eq} denotes distribution coefficient under thermodynamic equilibrium conditions, R_{net} is the net precipitation rate ($R_{net} = R_f + R_b$ with R_f and R_b standing for the forward and backward solid precipitation rate, respectively) and D_f is the forward kinetic distribution coefficient.

In the case of isotope fractionation Eq. (15) can be expressed as:

$$\alpha_{ss} = \frac{\alpha_f}{1 + \frac{R_b}{R_{net}+R_b}\left(\frac{\alpha_f}{\alpha_{eq}} - 1\right)} \quad (16)$$

where and α_f and α_{eq} denote the kinetic and equilibrium isotope fractionation factor, respectively. Note that when $R_{net} \to 0$, $\alpha_{ss} \to \alpha_{eq}$, and hence the equilibrium condition is achieved.

The use of Eqs. (15) and (16) for modelling of $D_{Sr,aragonite}$ and $\Delta^{88/86}Sr_{aragonite\text{-}fluid}$ as a function of growth rate is based upon the assumption of a diluted solid-solution formation where Sr is randomly distributed in the solid phase. Although each of Eqs. (15) and (16) requires the fitting of three parameters, in the case of Sr incorporation in aragonite in Eq. (15), D_f can be considered as being equal to 1 (see above). The best fits are summarized in Table 6 and can be seen in Fig. 8A ($D_{Sr,aragonite}$)

Table 6
Input parameters for Eqs. (13) and (14) that used for the fits displayed in Fig. 8.

	Fit 1	Fit 2	Fit 3
R_b (mol/m^2/s)	$10^{-7.6}$	$10^{-7.8}$	$10^{-7.9}$
D_{eq}	3	4	5
α_{eq}	0.99997	0.99999	0.99999
α_{kin}	0.9993	0.9994	0.9995

and Fig. 8B ($\Delta^{88/86}Sr_{aragonite\text{-}fluid}$). Note that for each fit the same R_b value was used in the fit of $D_{Sr,aragonite}$ and $\Delta^{88/86}Sr_{aragonite\text{-}fluid}$.

As can be seen in Fig. 8A, a value of the backward aragonite dissolution rate, R_b, of $10^{-7.6}$ to $10^{-7.9}$ (mol/m^2/s) together with a D_{eq} value ranging between 3 and 5 provide a reasonable fit to the $D_{Sr,aragonite}$ experimental data. The same range of R_b values and with almost constant α_{eq} equal to 0.999975 ± 0.000025 (i.e. −0.025 ± 0.015‰) can simulate the experimental $\Delta^{88/86}Sr_{aragonite\text{-}fluid}$ with α_f (i.e. the kinetic fractionation factor) ranging between 0.9993 and 0.9995 or 0.2‰. However, the best fit of both $D_{Sr,aragonite}$ and $\Delta^{88/86}Sr_{aragonite\text{-}fluid}$ experimental data is obtained for $R_b = 10^{-7.8}$ (mol/m^2/s) together with $D_{eq} = 4$, $\alpha_{eq} = 0.99999$ (−0.01‰) and $\alpha_f = 0.9994$ (−0.6‰). The D_{eq} value of 4 is somewhat higher, but within range to that estimated with Eq. (5) at $\Omega_{aragonite} = 1$. Moreover, the fitted α_f value is lower than the maximum α_f value proposed by Hofmann et al. (2012) for the kinetic fractionation factor associated with the dehydration of aqueous $^{88}Sr^{2+}$ and $^{86}Sr^{2+}$ ions based on molecular dynamic simulations ($\alpha_f = -1.1 \pm 0.2$‰). Similar discrepancy from the theoretical value of Hofmann et al. (2012) however, has been observed in the fitting by the SRKM of Ba isotope fractionation during aragonite growth (Mavromatis et al., 2020). Nevertheless, it can be suggested that Sr isotope fractionation during aragonite growth is associated with the slower rate of dehydration of the heavier ^{88}Sr isotope which results in preferential enrichment in the lighter ^{86}Sr at increasing precipitation rates.

The R_b value of $10^{-7.8\pm0.2}$ mol/m^2/s used in the present study to fit experimental data to Eqs. (13) and (14) is about one order of magnitude lower than that determined for aragonite dissolution in pure water by Cubillas et al. (2005) at the same pH and temperature. It is possible that the presence of strontium and magnesium in the reactive solutions slows down calcite/aragonite R_b values especially near equilibrium as demonstrated by Naviaux et al. (2019) who reported calcite R_b values in seawater of about $10^{-8.5}$ mol/m^2/s for $\Omega \geq 0.7$ (compared to $10^{-6.0}$ for $\Omega \sim 0$). Comparable decrease of aragonite R_b values have been recently deduced from Ca isotope exchange rates between aragonite and fluid at chemical equilibrium (Harrison et al., 2023). If R_b value decreases with increasing values of $\Omega_{aragonite}$, a somewhat different fit can be expected for Eqs. (15) and (16) which could affect the estimations of D_{eq} and α_f.

The observed $\Delta^{88/86}Sr_{aragonite\text{-}fluid}$ values of this study fall within the range of Sr isotope fractionation between Sr in aragonite and fluid reported in earlier experimental studies. For example, Fruchter et al. (2016) reported average $\Delta^{88/86}Sr_{aragonite\text{-}fluid}$ values of −0.171 ± 0.046‰ for synthetic aragonite formed from natural seawater, whereas AlKhatib and Eisenhauer (2017) report very similar $\Delta^{88/86}Sr_{aragonite\text{-}fluid}$ values of −0.218 ± 0.020‰ for experiments conducted at 25 °C. Interestingly, Fruchter et al. (2016) reports absence of growth rate impact effects on their $\Delta^{88/86}Sr_{aragonite\text{-}fluid}$, however, these authors do not provide surface normalized growth rates. The surface normalized growth rate dependence reported by AlKhatib and Eisenhauer (2017) is negligible compared to that observed in this study (see Fig. 4B). This difference can be attributed to the fact that the fluids from which aragonite formed in the study by AlKhatib and Eisenhauer (2017) are strongly supersaturated with respect to strontianite with $10^2 \leq \Omega_{SrCO3} \leq 10^{3.2}$ suggesting that this mineral phase is readily nucleating in their experiments and as such their results cannot reflect solely the presence of Sr in aragonite as a trace/impurity but rather the coprecipitation of strontianite and Sr-bearing aragonite. Actually, characteristic strontianite peaks have been identified in the XRD patterns presented by AlKhatib and Eisenhauer (2017). The formation of strontianite is characterized by larger enrichment in ^{86}Sr compared to that of aragonite as it is illustrated by earlier experimental works (e.g. Mavromatis et al., 2017; AlKhatib et al., 2022) and the DFT estimates of this study (Fig. 7).

4.4. Computational approach for modelling $\Delta^{88/86}Sr_{aragonite\text{-}fluid}$ and $\Delta^{88/86}Sr_{strontianite\text{-}fluid}$

In the modelling approach adopted herein, aqueous Sr^{2+} is modeled by inserting one Sr atom into a cubic box filled with water molecules and periodic boundary conditions are applied. The choice of the size of the simulation box defines the density of the fluid and therefore the pressure. With 1 Sr atom and 64 water molecules, a cubic box of 12.72 Å corresponds to a density of 1000 kg/m^3, i.e. the experimental water density at room temperature. However, the use of this box leads to an average pressure of −7 kbar instead of the expected atmospheric pressure of 1 bar, suggesting that the simulation box is too large for modeling ambient conditions. This finding is explained by the fact that Sr concentration in the experiments of this study (~0.2 mM) is several orders of magnitude smaller than in the simulation box, so the presence of Sr does not influence the fluid density. For this reason, a second approach has been adopted where the box volume and the atomic positions of each snapshot are optimized at the target pressure of 0.0 ± 0.2 kbar.

Comparing the DFT results with available data, it can be seen that the equilibrium isotope fractionation factor α_{eq} used in the surface kinetic model presented above (i.e. $\alpha_{eq} = 0.999975 \pm 0.000025$ corresponding to a fractionation of −0.025 ± 0.015‰) shows a good agreement with the same fractionation factor predicted by DFT calculations when the snapshots are relaxed at zero pressure (i.e. −0.04‰). Regarding the fractionation between strontianite and aqueous Sr^{2+}, DFT calculations predict a value of −0.13‰ becoming −0.29‰ at 298 K when snapshots are relaxed. This latter value is also in better agreement with the previous theoretical results of Widanagamage et al. (2014). In their study of Sr isotope fractionation in barite, they performed DFT calculations on strontianite, and modeled the aqueous Sr^{2+} ion with selected crystalline hydrates as analogues. After applying a scale factor, these authors found an isotopic fractionation between strontianite and fluid of −0.38‰ when taking the crystalline hydrate where Sr is 7-fold coordinated with water, while the same fractionation would become equal to ±0.05‰ for crystalline hydrates where Sr is 8-fold coordinated with water.

These comparisons tend to suggest that the second approach gives more satisfactory results. However, the refinement of the computational approach imposed by the relatively heavy mass of strontium must be put into perspective. As shown in Fig. 7, the difference between the results of the two approaches is 0.16‰ at 298 K. Although significant, this difference remains modest on the scale of the kinetic fractionations predicted by the surface kinetic model and by the dispersion of the experimental data around the fit of this model (Fig. 8).

5. Conclusions

In this study, the partition of Sr and its isotopic fractionation during its co-precipitation with aragonite at low degrees of supersaturation of the reacting fluid with respect to aragonite has been measured experimentally and theoretically approximated using first-principles calculations. The obtained results suggest that, in contrast to earlier works, Sr partition coefficient, $D_{Sr,aragonite}$, can achieve values significantly larger than one when mineral growth occurs at low $\Omega_{aragonite}$ values. Under increasing growth rate, however, $D_{Sr,aragonite}$ rapidly approaches a value of one, justifying the use of this parameter value for natural samples formed at far from chemical equilibrium conditions.

The $\Delta^{88/86}Sr_{aragonite\text{-}fluid}$ measured in the present study shows a quasi-constant value of −0.10 ± 0.05‰ at $r_p \leq 10^{-8.0}$ (mol/m^2/s) suggesting near isotope equilibrium conditions. This is supported by first-principles calculations showing a similar value for the equilibrium isotopic fractionation factor. Stable Sr isotope fractionation is strongly impacted by aragonite growth rate. Under the experimental conditions of this study, the value of the kinetic isotope fractionation factor used for modelling the obtained results with the SRK model by DePaolo (2011) was −0.6 ± 0.1‰, thus significantly higher than the value of −1.1‰ derived from the molecular dynamic simulations by Hofmann et al. (2012). Nevertheless, it is demonstrated that dehydration of the aqueous Sr^{2+} ions is the mechanism controlling Sr isotope fractionation during its co-precipitation with aragonite. The large variations with aragonite growth rate of $\Delta^{88/86}Sr_{aragonite\text{-}fluid}$ observed in this study together with

the high precision of stable Sr isotope measurements suggest that this isotopic system can be used to unravel formation conditions of natural aragonite samples.

Declaration of Competing Interest

The authors declare that they have no known competing financial interests or personal relationships that could have appeared to influence the work reported in this paper.

Acknowledgments

For their assistance with Sr isotope measurements, we acknowledge the help of Volker Liebetrau and Sophie Gangloff. Calculations were performed using the HPC resources from CALMIP (Grant 2022-P1037). The Raimond Castaing MicroCharacterization centre, particularly Arnaud Proietti, are thanked for their assistance with SEM analyses. We are thankful to the AE A. Jacobson and to Joji Uchikawa and two anonymous reviewers for their insightful comments that improved this manuscript. This study has been supported by the French national program INSU/LEFE and the Austrian FWF project P31832-N29.

Appendix A. Supplementary material

Figure S1 shows the dependence of growth rate of $\Omega_{aragonite}$ as it has been measured in this study and Fig. S7 presents the dependence of $D_{Sr,\ aragonite}$ on growth rate in the experiments of DeCarlo et al. (2015). Figures S2 to S6 include analytical measurements and results of theoretical calculations that support the DFT calculations of Sr equilibrium fractionation performed in this study. Table S1 includes the abundance of Ca and Sr aqueous species in the reactive fluids and Table S2 includes the Raman frequencies of aragonite and strontianite calculated in this study together with the experimental measurements of Lin and Liu (1997). Supplementary material to this article can be found online at https://doi.org/10.1016/j.gca.2023.08.013.

References

Alia, J.M., de Mera, Y.D., Edwards, H.G.M., Martin, P.G., Andres, S.L., 1997. FT-Raman and infrared spectroscopic study of aragonite-strontianite ($Ca_xSr_{1-x}CO_3$) solid solution. Spectroc. Acta Pt. A-Molec. Biomolec. Spectr. 53, 2347–2362.

AlKhatib, M., Eisenhauer, A., 2017. Calcium and strontium isotope fractionation during precipitation from aqueous solutions as a function of temperature and reaction rate; II. Aragonite. Geochim. Cosmochim. Acta 209, 320–342.

Alkhatib, M., Qutob, M., Alkhatib, S., Eisenhauer, A., 2022. Strontium isotope fractionation during precipitation of strontianite in aqueous solutions as a function of temperature and reaction rate. Chem. Geol. 587, 120625.

Antao, S.M., Hassan, I., 2009. The Orthorhombic Structure Of $CaCO_3$, $SrCO_3$, $PbCO_3$ and $BaCO_3$: Linear Structural Trends. Can. Mineral. 47, 1245–1255.

Bates, S.L., Hendry, K.R., Pryer, H.V., Kinsley, C.W., Pyle, K.M., Woodward, E.M.S., Horner, T.J., 2017. Barium isotopes reveal role of ocean circulation on barium cycling in the Atlantic. Geochim. Cosmochim. Acta 204, 286–299.

Beck, J.W., Edwards, R.L., Ito, E., Taylor, F.W., Recy, J., Rougerie, F., Joannot, P., Henin, C., 1992. Sea-surface temperature from coral skeletal strontium calcium ratios. Science 257, 644–647.

Beinlich, A., Austrheim, H., Mavromatis, V., Grguric, B., Putnis, C.V., Putnis, A., 2018. Peridotite weathering is the missing ingredient of Earth's continental crust composition. Nat. Commun. 9, 634.

Berendsen, H.J.C., Postma, J.P.M., van Gunsteren, W.F., DiNola, A., Haak, J.R., 1984. Molecular dynamics with coupling to an external bath. J. Chem. Phys. 81, 3684–3690.

Bigeleisen, J., Mayer, M.G., 1947. Calculation of equilibrium constants for isotopic exchange reactions. J. Chem. Phys. 15, 261–267.

Blanchard, M., Balan, E., Schauble, E.A., 2017. Equilibrium fractionation of non-traditional isotopes: A molecular modelling perspective. Rev. Min. Geochem. 82, 27–63.

Boehm, F., Eisenhauer, A., Tang, J., Dietzel, M., Krabbenhoeft, A., Kisakuerek, B., Horn, C., 2012. Strontium isotope fractionation of planktic foraminifera and inorganic calcite. Geochim. Cosmochim. Acta 93, 300–314.

Bogatko, S., Cauët, E., Bylaska, E., Schenter, G., Fulton, J., Weare, J., 2013. The aqueous Ca^{2+} system in comparison with Zn^{2+}, Fe^{3+}, and Al^{3+}: An ab initio molecular dynamic study. Chem. Eur. 19, 3047–3060.

Brazier, J.M., Mavromatis, V., 2022. Effect of growth rate on nickel and cobalt incorporation in aragonite. Chem. Geol. 600, 12.

Brazier, J.M., Schmitt, A.D., Gangloff, S., Pelt, E., Chabaux, F., Tertre, E., 2019. Calcium isotopic fractionation during adsorption onto and desorption from soil phyllosilicates (kaolinite, montmorillonite and muscovite). Geochim. Cosmochim. Acta 250, 324–347.

Brazier, J.M., Schmitt, A.D., Pelt, E., Lemarchand, D., Gangloff, S., Tacail, T., Balter, V., 2020a. Determination of radiogenic $^{87}Sr/^{86}Sr$ and Stable $\delta^{88/86}Sr$ SRM987 isotope values of thirteen mineral, vegetal and animal reference materials by DS-TIMS. Geostand. Geoanal. Res. 44, 331–348.

Brazier, J.M., Schmitt, A.D., Gangloff, S., Pelt, E., Gocke, M.I., Wiesenberg, G.L., 2020b. Multi-isotope approach ($\delta^{44/40}Ca$, $\delta^{88/86}Sr$ and $^{87}Sr/^{86}Sr$) provides insights into rhizolith formation mechanisms in terrestrial sediments of Nussloch (Germany). Chem. Geol. 545, 119641.

Brunauer, S., Emmett, P.H., Teller, E., 1938. Adsorption of gasses in multimolecular layers. J. Amer. Chem. Soc. 60, 309–319.

Bucca, M., Dietzel, M., Tang, J.W., Leis, A., Kohler, S.J., 2009. Nucleation and crystallization of otavite, witherite, calcite, strontianite, hydrozincite, and hydrocerussite by CO_2 membrane diffusion technique. Chem. Geol. 266, 143–156.

Busenberg, E., Plummer, L.N., Parker, V.B., 1984. The solubility of strontianite ($SrCO_3$) in CO_2-H_2O solutions between 2 and 91°C, the association constants of $SrHCO_3^+$ (aq) and $SrCO_3^0$ (aq) between 5 and 80 °C, and an evaluation of the thermodynamic properties of Sr^{2+} (aq) and $SrCO_3$(cr) at 25 °C and 1 atm total pressure. Geochim. Cosmochim. Acta 48, 2021–2035.

Casey, W.H., Chai, L.A., Navrotsky, A., Rock, P.A., 1996. Thermochemistry of mixing strontianite $SrCO_3$(s) and aragonite $CaCO_3$(s) to form $Ca_xSr_{1-x}CO_3$(s) solid solutions. Geochim. Cosmochim. Acta 60, 933–940.

Castillo-Alvarez, C., Quitte, G., Schott, J., Oelkers, E.H., 2021. Nickel isotope fractionation as a function of carbonate growth rate during Ni coprecipitation with calcite. Geochim. Cosmochim. Acta 299, 184–198.

Cohen, A.L., McConnaughey, T.A., 2003. Geochemical perspectives on coral mineralization. Rev. Min. Geochem 54, 151–187.

Cubillas, P., Koehler, S., Prieto, M., Chairat, C., Oelkers, E.H., 2005. Experimental determination of the dissolution rates of calcite, aragonite, and bivalves. Chem. Geol. 216, 59–77.

de Villiers, S., Nelson, B.K., Chivas, A.R., 1995. Biological-controls on coral Sr/Ca and $\delta^{18}O$ reconstructions of sea-surface temperatures. Science 269, 1247–1249.

DeCarlo, T.M., Gaetani, G.A., Holcomb, M., Cohen, A.L., 2015. Experimental determination of factors controlling U/Ca of aragonite precipitated from seawater: Implications for interpreting coral skeleton. Geochim. Cosmochim. Acta 162, 151–165.

DeCarlo, T.M., D'Olivo, J.P., Foster, T., Holcomb, M., Becker, T., McCulloch, M.T., 2017. Coral calcifying fluid aragonite saturation states derived from Raman spectroscopy. Biogeosciences 14, 5253–5269.

DePaolo, D.J., 2011. Surface kinetic model for isotopic and trace element fractionation during precipitation of calcite from aqueous solutions. Geochim. Cosmochim. Acta 75, 1039–1056.

Dietzel, M., Gussone, N., Eisenhauer, A., 2004. Co-precipitation of Sr^{2+} and Ba^{2+} with aragonite by membrane diffusion of CO_2 between 10 and 50 °C. Chem. Geol. 203, 139–151.

Dromgoole, E.L., Walter, L.M., 1990. Iron and manganese Incorporation Into calcite - Effects of growth-kinetics, temperature and solution chemistry. Chem. Geol. 81, 311–336.

Ducher, M., Blanchard, M., Balan, E., 2016. Equilibrium zinc isotope fractionation in Zn-bearing minerals from first-principles calculations. Chem. Geol. 443, 87–96.

Farfan, G.A., Cordes, E.E., Waller, R.G., DeCarlo, T.M., Hansel, C.M., 2018. Mineralogy of Deep-Sea coral aragonites as a function of aragonite saturation state. Front. Mar. Sci. 5, 15.

Farmer, J.R., Branson, O., Uchikawa, J., Penman, D.E., Honisch, B., Zeebe, R.E., 2019. Boric acid and borate incorporation in inorganic calcite inferred from B/Ca, boron isotopes and surface kinetic modeling. Geochim. Cosmochim. Acta 244, 229–247.

Feely, R.A., Doney, S.C., Cooley, S.R., 2009. Ocean acidification: Present conditions and future changes in a high-CO_2 world. Oceanography 22, 36–47.

Ferrier-Pages, C., Boisson, F., Allemand, D., Tambutte, E., 2002. Kinetics of strontium uptake in the scleractinian coral Stylophora *pistillata*. Mar. Ecol.-Prog. Ser. 245, 93–100.

Fietzke, J., Eisenhauer, A., 2006. Determination of temperature-dependent stable strontium isotope ($^{88}Sr/^{86}Sr$) fractionation via bracketing standard MC-ICP-MS. Geochem. Geophys. Geosyst. 7, 6.

Finch, A.A., Allison, N., 2003. Strontium in coral aragonite: 2. Sr coordination and the long-term stability of coral environmental records. Geochim. Cosmochim. Acta 67, 4519–4527.

Foster, L.C., Allison, N., Finch, A.A., Andersson, C., 2009. Strontium distribution in the shell of the aragonite bivalve Arctica islandica. Geochem. Geophys. Geosyst. 10, 14.

Fruchter, N., Eisenhauer, A., Dietzel, M., Fietzke, J., Bohm, F., Montagna, P., Stein, M., Lazar, B., Rodolfo-Metalpa, R., Erez, J., 2016. $^{88}Sr/^{86}Sr$ fractionation in inorganic aragonite and in corals. Geochim. Cosmochim. Acta 178, 268–280.

Füger, A., Bruggmann, S., Frei, R., Leis, A., Dietzel, M., Mavromatis, V., 2019. The role of pH on Cr(VI) partitioning and isotopic fractionation during its incorporation in calcite. Geochim. Cosmochim. Acta 265, 520–532.

Füger, A., Kuessner, M., Rollion-Bard, C., Leis, A., Magna, T., Dietzel, M., Mavromatis, V., 2022. Effect of growth rate and pH on Li isotope fractionation during its incorporation in calcite. Geochim. Cosmochim. Acta 323, 276–290.

Gaetani, G.A., Cohen, A.L., 2006. Element partitioning during precipitation of aragonite from seawater: A framework for understanding paleoproxies. Geochim. Cosmochim. Acta 70, 4617–4634.

Gautier, Q., Bénézeth, P., Mavromatis, V., Schott, J., 2014. Hydromagnesite solubility product and growth kinetics in aqueous solution from 25 to 75°C. Geochim. Cosmochim. Acta 138, 1–20.
Giannozzi, P., Baroni, S., Bonini, N., Calandra, M., Car, R., Cavazzoni, C., Ceresoli, D., Chiarotti, G.L., Cococcioni, M., Dabo, I., Dal Corso, A., de Gironcoli, S., Fabris, S., Fratesi, G., Gebauer, R., Gerstmann, U., Gougoussis, C., Kokalj, A., Lazzeri, M., Martin-Samos, L., Marzari, N., Mauri, F., Mazzarello, R., Paolini, S., Pasquarello, A., Paulatto, L., Sbraccia, C., Scandolo, S., Sclauzero, G., Seitsonen, A.P., Smogunov, A., 2009. QUANTUM ESPRESSO: a modular and open-source software project for quantum simulations of materials. J. Phys. Condens. Matter 21, 395502.
Gillikin, D.P., Lorrain, A., Navez, J., Taylor, J.W., André, L., Keppens, E., Baeyens, W., Dehairs, F., 2005. Strong biological controls on Sr/Ca ratios in aragonitic marine bivalve shells. Geochem. Geophys. Geosyst. 6.
Goetschl, K.E., Purgstaller, B., Dietzel, M., Mavromatis, V., 2019. Effect of sulfate on magnesium incorporation in low-magnesium calcite. Geochim. Cosmochim. Acta 265, 505–519.
Greegor, R.B., Pingitore, N.E., Lytle, F.W., 1997. Strontianite in coral skeletal aragonite. Science 275, 1452–1454.
Harrison, A.L., Mavromatis, V., Oelkers, E.H., Benezeth, P., 2019. Solubility of the hydrated Mg-carbonates nesquehonite and dypingite from 5 to 35 °C: Implications for CO_2 storage and the relative stability of Mg-carbonates. Chem. Geol. 504, 123–135.
Harrison, A.L., Benezeth, P., Schott, J., Oelkers, E.H., Mavromatis, V., 2021. Magnesium and carbon isotope fractionation during hydrated Mg-carbonate mineral phase transformations. Geochim. Cosmochim. Acta 293, 507–524.
Harrison, A.L., Heuser, A., Liebetrau, V., Eisenhauer, A., Schott, J., Mavromatis, V., 2023. Equilibrium Ca isotope fractionation and the rates of isotope exchange in the calcite-fluid and aragonite-fluid systems at 25 °C. Earth Planet. Sci. Lett. 603, 117985.
Henderson, L.M., Kracek, F.C., 1927. The fractional precipitation of barium and radium chromates. J. Am. Chem. Soc. 49, 739–749.
Henehan, M.J., Gebbinck, C.D.K., Wyman, J.V.B., Hain, M.P., Rae, J.W.B., Honisch, B., Foster, G.L., Kim, S.T., 2022. No ion is an island: Multiple ions influence boron incorporation into $CaCO_3$. Geochim. Cosmochim. Acta 318, 510–530.
Hofmann, A.E., Bourg, I.C., DePaolo, D.J., 2012. Ion desolvation as a mechanism for kinetic isotope fractionation in aqueous systems. Proc. Nat. Acad. Sci. 109, 18689–18694.
Horner, T.J., Kinsley, C.W., Nielsen, S.G., 2015. Barium-isotopic fractionation in seawater mediated by barite cycling and oceanic circulation. Earth Planet. Sci. Lett. 430, 511–522.
Ikeda, T., Boero, M., Terakura, K., 2007. Hydration properties of magnesium and calcium ions from constrained first principles molecular dynamics. J. Chem. Phys. 127, 074503.
Krabbenhoft, A., Fietzke, J., Eisenhauer, A., Liebetrau, V., Bohm, F., Vollstaedt, H., 2009. Determination of radiogenic and stable strontium isotope ratios ($^{87}Sr/^{86}Sr$; $\delta^{88/86}Sr$ by thermal ionization mass spectrometry applying an $^{87}Sr/^{84}Sr$ double spike. J. Anal. At. Spectrom 24, 1267–1271.
Kulik, D.A., Vinograd, V.L., Paulsen, N., Winkler, B., 2010. (Ca, Sr)C_O3 aqueous-solid solution systems: From atomistic simulations to thermodynamic modelling. Phys. Chem. Earth 35, 217–232.
Lakshtanov, L.Z., Stipp, S.L.S., 2007. Experimental study of nickel(II) interaction with calcite: Adsorption and coprecipitation. Geochim. Cosmochim. Acta 71, 3686–3697.
Lammers, L.N., Kulasinskki, K., Zarzycki, P., DePaolo, D.J., 2020. Molecular simulations of kinetic stable calcium isotope fractionation at the calcite aqueous interface. Chem. Geol. 532, 119315.
Lee, Y.J., Reeder, R.J., 2006. The role of citrate and phthalate during Co(II) coprecipitation with calcite. Geochim. Cosmochim. Acta 70, 2253–2263.
Lin, C.-C., Liu, L.-G., 1997. Post-aragonite phase transitions in strontianite and cerussite – A high-pressure Raman spectroscopic study. J. Phys. Chem. Solid 58, 977–987.
Lorens, R.B., 1981. Sr, Cd, Mn and Co distribution coefficient in calcite as a function of calcite precipitation rate. Geochim. Cosmochim. Acta 45, 553–561.
Marshall, J.F., McCulloch, M.T., 2002. An assessment of the Sr/Ca ratio in shallow water hermatypic corals as a proxy for sea surface temperature. Geochim. Cosmochim. Acta 66, 3263–3280.
Mavromatis, V., Pearce, C.R., Shirokova, L.S., Bundeleva, I.A., Pokrovsky, O.S., Benezeth, P., Oelkers, E.H., 2012. Magnesium isotope fractionation during hydrous magnesium carbonate precipitation with and without cyanobacteria. Geochim. Cosmochim. Acta 76, 161–174.
Mavromatis, V., Montouillout, V., Noireaux, J., Gaillardet, J., Schott, J., 2015. Characterization of boron incorporation and speciation in calcite and aragonite from co-precipitation experiments under controlled pH, temperature and precipitation rate. Geochim. Cosmochim. Acta 150, 299–313.
Mavromatis, V., Harrison, A.L., Eisenhauer, A., Dietzel, M., 2017. Strontium isotope fractionation during strontianite ($SrCO_3$) dissolution, precipitation and at equilibrium. Geochim. Cosmochim. Acta 218, 201–214.
Mavromatis, V., Gautier, Q., Bosc, O., Schott, J., 2013. Kinetics of Mg partition and Mg stable isotope fractionation during its incorporation in calcite. Geochim. Cosmochim. Acta 114, 188–203.
Mavromatis, V., Goetschl, K.E., Grengg, C., Konrad, F., Purgstaller, B., Dietzel, M., 2018. Barium partitioning in calcite and aragonite as a function of growth rate. Geochim. Cosmochim. Acta 237, 65–78.
Mavromatis, V., Gonzalez, A.G., Dietzel, M., Schott, J., 2019. Zinc isotope fractionation during the inorganic precipitation of calcite - Towards a new pH proxy. Geochim. Cosmochim. Acta 244, 99–112.
Mavromatis, V., Purgstaller, B., Louvat, P., Faure, L., Montouillout, V., Gaillardet, J., Schott, J., 2021. Boron isotope fractionation during the formation of amorphous calcium carbonates and their transformation to Mg-calcite and aragonite. Geochim. Cosmochim. Acta 315, 152–171.
Mavromatis, V., Brazier, J.M., Goetschl, K.E., 2022. Controls of temperature and mineral growth rate on Mg incorporation in aragonite. Geochim. Cosmochim. Acta 317, 53–64.
Mavromatis, V., van Zuilen, K., Blanchard, M., van Zuilen, M., Dietzel, M., Schott, J., 2020. Experimental and theoretical modelling of kinetic and equilibrium Ba isotope fractionation during calcite and aragonite precipitation. Geochim. Cosmochim. Acta 269, 566–580.
Mills, J.V., DePaolo, D.J., Lammers, L.N., 2021. The influence of Ca:CO_3 stoichiometry on Ca isotope fractionation: Implications for process-based models of calcite growth. Geochim. Cosmochim. Acta 298, 87–111.
Monkhorst, H.J., Pack, J.D., 1976. Special points for Brillouin-zone integrations. Phys. Rev. B 13, 5188–5192.
Moreau, G., Helm, L., Purans, J., Merbach, A.E., 2002. Structural investigation of the aqueous Eu^{2+} ion: Comparison with Sr^{2+} using the XAFS technique. Chem. A Eur. J. 106, 3034–3043.
Morse, J.W., 1983. The kinetics of calcium carbonate dissolution and precipitation. Rev. Mineral. Geochem. 11, 227–264.
Morse, J.W., MacKenzie, F.T., 1990. Geochemistry of Sedimentary Carbonates. Elsevier.
Naviaux, J.D., Subhas, A.V., Rollins, N.E., Dong, S., Berelson, W.M., Adkins, J.F., 2019. Temperature dependence of calcite dissolution kinetics in seawater. Geochim. Cosmochim. Acta 246, 363–384.
Nielsen, L.C., DePaolo, D.J., De Yoreo, J.J., 2012. Self-consistent ion-by-ion growth model for kinetic isotopic fractionation during calcite precipitation. Geochim. Cosmochim. Acta 86, 166–181.
Noireaux, J., Mavromatis, V., Gaillardet, J., Schott, J., Montouillout, V., Louvat, P., Rollion-Bard, C., Neuville, D.R., 2015. Crystallographic control on the boron isotope paleo-pH proxy. Earth Planet. Sci. Lett. 430, 398–407.
Parkhurst, D.L., Appelo, C.A.J., 2013. Description of input and examples for PHREEQC version 3: a computer program for speciation, batch-reaction, one-dimensional transport, and inverse geochemical calculations (No. 6-A43). US Geological Survey.
Pearce, C.R., Saldi, G.D., Schott, J., Oelkers, E.H., 2012. Isotopic fractionation during congruent dissolution, precipitation and at equilibrium: Evidence from Mg isotopes. Geochim. Cosmochim. Acta 92, 170–183.
Perdew, J.P., Burke, K., Ernzerhof, M., 1996. Generalized gradient approximation made simple. Phys. Rev. Lett. 77, 3865–3868.
Plummer, L.N., Busenberg, E., 1982. The solubilities of calcite, aragonite and vaterite in CO_2-H_2O solutions between 0 and 90 °C, and an evaluation of the aqueous model for the system $CaCO_3$-CO_2-H_2O. Geochim. Cosmochim. Acta 46, 1011–1040.
Plummer, L.N., Busenberg, E., 1987. Thermodynamics of aragonite-strontianite solid solutions: Results from stoichiometric solubility at 25 and 76 °C. Geochim. Cosmochim. Acta 51, 1393–1411.
Plummer, L.N., Busenberg, E., Glynn, P.D., Blum, A.E., 1992. Dissolution of aragonite-strontianite solid-solutions in nonstoichiometric $Sr(HCO_3)_2$-$Ca(HCO_3)_2$-CO_2-H_2O solutions. Geochim. Cosmochim. Acta 56, 3045–3072.
Pokrovsky, O.S., Schott, J., 2002. Surface chemistry and dissolution kinetics of divalent metal carbonates. Environ. Sci. Tech. 36 (3), 426–432.
Raddatz, J., Liebetrau, V., Ruggeberg, A., Hathorne, E., Krabbenhoft, A., Eisenhauer, A., Bohm, F., Vollstaedt, H., Fietzke, J., Lopez Correa, M., Freiwald, A., Dullo, W.C., 2013. Stable Sr-isotope, Sr/Ca, Mg/Ca, Li/Ca and Mg/Li ratios in the scleractinian cold-water coral Lophelia *pertusa*. Chem. Geol. 352, 143–152.
Ruggeberg, A., Fietzke, J., Liebetrau, V., Eisenhauer, A., Dullo, W.C., Freiwald, A., 2008. Stable strontium isotopes ($\delta^{88/86}Sr$) in cold-water corals - A new proxy for reconstruction of intermediate ocean water temperatures. Earth Planet. Sci. Lett. 269, 569–574.
Ruiz-Hernandez, S.E., Grau-Crespo, R., Ruiz-Salvador, A.R., De Leeuw, N.H., 2010. Thermochemistry of strontium incorporation in aragonite from atomistic simulations. Geochim. Cosmochim. Acta 74, 1320–1328.
Saxena, S.K., 1973. Thermodynamics of Rock-Forming Crystalline Solutions. Springer-Verlag.
Schlipf, M., Gygi, F., 2015. Optimization algorithm for the generation of ONCV pseudopotentials. Comput. Phys. Commun. 196, 36–44.
Schmidt, G.A., 1999. Error analysis of paleosalinity calculations. Paleoceanography 14, 422–429.
Schmitt, A.D., Gangloff, S., Labolle, F., Chabaux, F., Stille, P., 2017. Calcium biogeochemical cycle at the beech tree-soil solution interface from the Strengbach CZO (NE France): insights from stable Ca and radiogenic Sr isotopes. Geochim. Cosmochim. Acta 213, 91–109.
Schott, J., Pokrovsky, O.S., Oelkers, E.H., 2009. The link between mineral dissolution/precipitation kinetics and solution chemistry. Rev. Min. Geochem. 70, 207–258.
Schott, J., Mavromatis, V., Fujii, T., Pearce, C.R., Oelkers, E.H., 2016. The control of carbonate mineral Mg isotope composition by aqueous speciation: Theoretical and experimental modelling. Chem. Geol. 445, 120–134.
Shannon, R.D., 1976. Revised effective ionic radii and systematic studies of interatomic distances in halides and chalcogenides. Acta Crystallogr. Sect. A: Cryst. Phys., Diffr., Theor. Gen. Crystallogr. 32 (5), 751–767.
Speer, 1983. Crystal chemistry and phase relations of orthorhombic carbonates. In: Reeder, R.J. (Ed.), Reviews in Mineralogy: Carbonates–Mineralogy and Chemistry, pp. 145–189.
Tang, J., Koehler, S.J., Dietzel, M., 2008. Sr2+/Ca2+ and 44Ca/40Ca fractionation during inorganic calcite formation: I. Sr incorporation. Geochim. Cosmochim. Acta 72 (15), 3718–3732.
Uchikawa, J., Penman, D.E., Harper, D.T., Farmer, J.R., Zachos, J.C., Planavsky, N.J., Zeebe, R.E., 2023. Sulfate and phosphate oxyanions alter B/Ca and $\delta^{11}B$ in inorganic

calcite at constant pH: Crystallographic controls outweigh normal kinetic effects. Geochim. Cosmochim. Acta 343, 353–370.
Voigt, M., Mavromatis, V., Oelkers, E.H., 2017. The experimental determination of REE partition coefficients in the water-calcite system. Chem. Geol. 462, 30–43.
Wang, X., Wang, Z.R., Zhu, X., Liu, D., Miao, Y.F., Ye, Y., 2021. X-ray diffraction and spectroscopic study of $Sr_xCa_{1-x}CO_3$: Implications for equilibrium Sr^{2+} incorporation and carbon/oxygen isotope fractionation in aragonite. Geochim. Cosmochim. Acta 309, 112–134.
Wassenburg, J.A., Scholz, D., Jochum, K.P., Cheng, H., Oster, J., Immenhauser, A., Richter, D.K., Hager, T., Jamieson, R.A., Baldini, J.U.L., Hoffmann, D., Breitenbach, S.F.M., 2016. Determination of aragonite trace element distribution coefficients from speleothem calcite-aragonite transitions. Geochim. Cosmochim. Acta 190, 347–367.
Widanagamage, I.H., Schauble, E.A., Scher, H.D., Griffith, E.M., 2014. Stable strontium isotope fractionation in synthetic barite. Geochim. Cosmochim. Acta 147, 58–75.
Zhong, S., Mucci, A., 1989. Calcite and aragonite precipitation from seawater solutions of various salinities; precipitation rates and overgrowth compositions. Chem. Geol. 78, 283–299.